UNIVERSIDADE DE SÃO PAULO
Instituto de Ciências Matemáticas e de Computação
ISSN 0103-2577

A MARKER-AND-CELL TECHNIQUE FOR SIMULATING UNSTEADY VISCOELASTIC FREE SURFACE FLOWS

M.F. TOMÉ
N. MANGIAVACCHI.
J.A. CUMINATO
A. CASTELO
S. MCKEE

Nº 63

NOTAS DO ICMC

SÉRIE COMPUTAÇÃO

São Carlos – SP
Nov./2011

SYSNO 1291728
DATA / /
ICMC - SBAB

A Marker-and-Cell Technique for Simulating Unsteady Viscoelastic Free Surface Flows

M. F. Tomé, N. Mangiavacchi, J. A. Cuminato, A. Castelo

Departamento de Ciências da Computação e Estatística
Instituto de Ciências Matemáticas e de Computação
Universidade de São Paulo - Campus de São Carlos
Caixa Postal 668
13560-970 São Carlos - SP

S. McKee

Department of Mathematics
University of Strathclyde
Richmond Street, 26
G1 1XH - Glasgow - UK.

Resumo

Esse trabalho apresenta um método numérico para resolver escoamentos viscoelásticos com superfícies livres. As equações que governam o escoamento de um fluido tipo Oldroyd-B são consideradas. Um novo tratamento para o cálculo das componentes do tensor extra-tensão em contôrnos rígidos é apresentado em detalhes. As condições de contôrno na superfície livre são aplicadas sem recorrer a simplificações. As equações governantes são resolvidas pelo método de diferenças finitas numa malha diferenciada. Resultados numéricos demonstrando a capacidade desse novo método numérico para resolver escoamentos viscoelásticos são apresentados.

Abstract

This work is concerned with the development of a numerical method capable of simulating viscoelastic free surface flow of an Oldroyd-B fluid. The basic equations governing the flow of an Oldroyd-B fluid are considered. A novel formulation is developed for the computation of the non-Newtonian extra-stress components on rigid boundaries. The full free surface stress conditions are employed. The resulting governing equations are solved by a finite difference method on a staggered grid, influenced by the ideas of the marker-and-cell (MAC) method. Numerical results demonstrating the capabilities of this new technique are presented for a number of problems involving unsteady free surface flows.

KEY WORDS: Viscoelastic flow, Oldroyd-B, finite difference, constitutive equations

1. Introduction

A great deal of effort has been expended over the last 15 years or so in attempting to find robust and stable numerical methods for viscoelastic flow problems. The models that have been studied tend to be the classical Oldroyd-B model or the upper convected Maxwell model with the constitutive equation either of differential or integral form. Numerical methods have included finite difference methods (eg. Yoo and Na [1]), finite element methods (eg. Marchal and Crochet [2], Carew et al. [3], Brasseur et al. [4]), finite volume methods (eg. Huang et al. [5], Mompean and Deville [6], Xue et al. [7], Phillips and Williams [8]), spectral methods (eg. Beris et al. [9]), and boundary integral methods (eg. Fan et al.[10]) and there now exists some measure of agreement for a class of test problems. These test problems have arisen because of the so called "High Weissenberg Number Problem". Rather like the Reynolds number in Newtonian fluids, it has been found that a Weissenberg number is eventually reached above which convergence of the numerical method under consideration fails. And indeed this number was not very large and nearly all existing codes have difficulty with a Weissenberg number greater than about 4 (however, see Mompean and Deville [6]). In this paper viscoelastic flows with multiple free surfaces are considered. The approach employed is loosely based upon the marker-and-cell (MAC) ideas of Harlow and Welch [11] and has been honed for many problems in Newtonian fluid mechanics (see eg. Tomé and McKee [12], Castelo et al. [13], Tomé et al. [14] and Tomé et al. [20]). It has also proved effective for solving generalised non-Newtonian fluid flow (see eg. Tomé et al. [25]).

We should say at this point that fluid flow with a free surface (or surfaces) is a very active research area among the Newtonian fluid mechanics community. The main focus has been on tracking, or capturing the free surface, or in the case of multiphase flows, the material interface. Indeed, interface tracking methods may be classified into three types. The first involves finding a piecewise polynomial to approximate the front. This class includes boundary integral methods (eg. Oguz et al. [22]) and the methods of Glimm and McBrian [22], Agresar et al. [23], and Udaykumar et al. [24]. The second is the so-called level set methods introduced by Osher and Sethian [15] and described in detail in two books by Sethian [16], [17]. The third approach is the so-called volume of fluid (VOF) that is used in the code FLOW3D (Hirt [18]); higher order approximations have been recently proposed by Puckett et al. [19].

This paper is, we believe, one of the first to treat viscoelastic free surface flow problems. The method described herein is applied to Couette flow, jet impingement and extrudate swell. The Couette flow results agrees with those of Mompean and Deville [6] and the analytic solution of Schaftingen [30]. The paper is organised as follows. The governing equations are set out. The boundary conditions, especially for the non-Newtonian contribution to the extra-stress tensor, are discussed at length. The essence of the method is given in Section 4 while in Section 5, the basic finite difference discretization is discussed. Section 6 includes some general comments and Section 7 provides validation results for channel flow and a start-up Couette flow. Section 8 presents some numerical results and finally, Section 9 completes

the paper with some concluding remarks.

2. Governing equations

The basic equations governing the flow of an Oldroyd B fluid are (see Crochet, Davies and Walters [26]) the constitutive equations

$$T_{ik} + \lambda_1 \overset{\nabla}{T}_{ik} = 2\mu_0 \left(d_{ik} + \lambda_2 \overset{\nabla}{d}_{ik} \right) \tag{1}$$

together with the equation of motion

$$\rho \frac{Dv_i}{Dt} = -\frac{\partial p}{\partial x_i} + \frac{\partial T_{ik}}{\partial x_k} + \rho g_i \tag{2}$$

and the continuity equation (assuming incompressibility)

$$\frac{\partial v_i}{\partial x_i} = 0 \tag{3}$$

where T_{ik} is the symmetric extra-stress tensor. The upper convected derivative $\overset{\nabla}{T}_{ik}$ is defined by

$$\overset{\nabla}{T}_{ik} = \frac{\partial T_{ik}}{\partial t} + v_m \frac{\partial T_{ik}}{\partial x_m} - \frac{\partial v_i}{\partial x_m} T_{mk} - \frac{\partial v_k}{\partial x_m} T_{im}$$

and

$$d_{ik} = \frac{1}{2} \left(\frac{\partial v_i}{\partial x_k} + \frac{\partial v_k}{\partial x_i} \right)$$

is the rate-of-deformation tensor and λ_1 and λ_2 are time constants (retardation) and μ_0 is the solvent viscosity. The vector $v_i, (i = 1, 2)$ denotes the velocity, p the pressure, ρ the density and $g_i, (i = 1, 2)$ the components of gravity. $\frac{D}{Dt}$ denotes the material derivative. We observe that by making $\lambda_2 = 0$ we obtain the Maxwell model. In order to solve (1)–(3) we introduce the splitting

$$T_{ik} = 2\mu_0 \left(\frac{\lambda_2}{\lambda_1} \right) d_{ik} + S_{ik} \tag{4}$$

where S_{ik} represents the non-Newtonian contribution to the extra-stress tensor. By introducing (4) into (1) and (2) we get

$$S_{ik} + \lambda_1 \overset{\nabla}{S}_{ik} = 2\mu_0 \left(1 - \frac{\lambda_2}{\lambda_1} \right) d_{ik} \tag{5}$$

$$\rho \frac{Dv_i}{Dt} = -\frac{\partial p}{\partial x_i} + \mu_0 \left(\frac{\lambda_2}{\lambda_1} \right) \frac{\partial}{\partial x_k} \left(\frac{\partial v_i}{\partial x_k} + \frac{\partial v_k}{\partial x_i} \right) + \frac{\partial S_{ik}}{\partial x_k} + \rho g_i \tag{6}$$

If we consider two-dimensional Cartesian coordinates then equations (5), (6) and (3) can be written in the form

$$S^{xx}+\lambda_1\left(\frac{\partial S^{xx}}{\partial t}+u\frac{\partial S^{xx}}{\partial x}+v\frac{\partial S^{xx}}{\partial y}-2\frac{\partial u}{\partial x}S^{xx}-2\frac{\partial u}{\partial y}S^{xy}\right) = 2\mu_0\left(1-\frac{\lambda_2}{\lambda_1}\right)\frac{\partial u}{\partial x} \quad (7)$$

$$S^{yy}+\lambda_1\left(\frac{\partial S^{yy}}{\partial t}+u\frac{\partial S^{yy}}{\partial x}+v\frac{\partial S^{yy}}{\partial y}-2\frac{\partial v}{\partial x}S^{xy}-2\frac{\partial v}{\partial y}S^{yy}\right) = 2\mu_0\left(1-\frac{\lambda_2}{\lambda_1}\right)\frac{\partial v}{\partial y} \quad (8)$$

$$S^{xy}+\lambda_1\left(\frac{\partial S^{xy}}{\partial t}+u\frac{\partial S^{xy}}{\partial x}+v\frac{\partial S^{xy}}{\partial y}-\frac{\partial v}{\partial x}S^{xx}-\frac{\partial u}{\partial y}S^{yy}\right) = \mu_0\left(1-\frac{\lambda_2}{\lambda_1}\right)\left(\frac{\partial u}{\partial y}+\frac{\partial v}{\partial x}\right) \quad (9)$$

$$\frac{\partial u}{\partial t}+\frac{\partial u^2}{\partial x}+\frac{\partial (uv)}{\partial y}=-\frac{1}{\rho}\frac{\partial p}{\partial x}+\nu_0\left(\frac{\lambda_2}{\lambda_1}\right)\left(\frac{\partial^2 u}{\partial x^2}+\frac{\partial^2 u}{\partial y^2}\right)+\frac{1}{\rho}\left(\frac{\partial S^{xx}}{\partial x}+\frac{\partial S^{xy}}{\partial y}\right)+g_x \quad (10)$$

$$\frac{\partial v}{\partial t}+\frac{\partial (uv)}{\partial x}+\frac{\partial v^2}{\partial y}=-\frac{1}{\rho}\frac{\partial p}{\partial y}+\nu_0\left(\frac{\lambda_2}{\lambda_1}\right)\left(\frac{\partial^2 v}{\partial x^2}+\frac{\partial^2 v}{\partial y^2}\right)+\frac{1}{\rho}\left(\frac{\partial S^{xy}}{\partial x}+\frac{\partial S^{yy}}{\partial y}\right)+g_y \quad (11)$$

$$\frac{\partial u}{\partial x}+\frac{\partial v}{\partial y}=0 \quad (12)$$

respectively. In equations above, $\nu_0=\mu_0/\rho$ is the kinematic viscosity and g_x, g_y are the gravity components in the x and y directions respectively.

By letting L, U and ν_0 denote "typical" length, velocity and viscosity scales, we introduce the nondimensionalization

$$u=U\bar{u},\ v=U\bar{v},\ x=L\bar{x},\ y=L\bar{y},\ t=\frac{L}{U}\bar{t},\ p=\rho U^2\bar{p},\ \nu=\nu_0\bar{\nu},\ S_{ik}=(\mu_0 U/L)\,\bar{S}_{ik},\ \mathbf{g}=g\bar{\mathbf{g}},$$

which upon introduction into (7)–(12) produces the following nondimensional equations (the bars have been dropped for convenience)

$$S^{xx}+We\left(\frac{\partial S^{xx}}{\partial t}+u\frac{\partial S^{xx}}{\partial x}+v\frac{\partial S^{xx}}{\partial y}-2\frac{\partial u}{\partial x}S^{xx}-2\frac{\partial u}{\partial y}S^{xy}\right) = 2\left(1-\frac{\lambda_2}{\lambda_1}\right)\frac{\partial u}{\partial x} \quad (13)$$

$$S^{yy}+We\left(\frac{\partial S^{yy}}{\partial t}+u\frac{\partial S^{yy}}{\partial x}+v\frac{\partial S^{yy}}{\partial y}-2\frac{\partial v}{\partial x}S^{xy}-2\frac{\partial v}{\partial y}S^{yy}\right) = 2\left(1-\frac{\lambda_2}{\lambda_1}\right)\frac{\partial v}{\partial y} \quad (14)$$

$$S^{xy}+We\left(\frac{\partial S^{xy}}{\partial t}+u\frac{\partial S^{xy}}{\partial x}+v\frac{\partial S^{xy}}{\partial y}-\frac{\partial v}{\partial x}S^{xx}-\frac{\partial u}{\partial y}S^{yy}\right) = \left(1-\frac{\lambda_2}{\lambda_1}\right)\left(\frac{\partial u}{\partial y}+\frac{\partial v}{\partial x}\right) \quad (15)$$

$$\frac{\partial u}{\partial t}+\frac{\partial u^2}{\partial x}+\frac{\partial (uv)}{\partial y} = -\frac{\partial p}{\partial x}+\frac{1}{Re}\left(\frac{\lambda_2}{\lambda_1}\right)\left(\frac{\partial^2 u}{\partial x^2}+\frac{\partial^2 u}{\partial y^2}\right)+\frac{1}{Re}\left(\frac{\partial S^{xx}}{\partial x}+\frac{\partial S^{xy}}{\partial y}\right)+\frac{1}{F_r^2}g_x \quad (16)$$

$$\frac{\partial v}{\partial t}+\frac{\partial (uv)}{\partial x}+\frac{\partial v^2}{\partial y} = -\frac{\partial p}{\partial y}+\frac{1}{Re}\left(\frac{\lambda_2}{\lambda_1}\right)\left(\frac{\partial^2 v}{\partial x^2}+\frac{\partial^2 v}{\partial y^2}\right)+\frac{1}{Re}\left(\frac{\partial S^{xy}}{\partial x}+\frac{\partial S^{yy}}{\partial y}\right)+\frac{1}{F_r^2}g_y \quad (17)$$

$$\frac{\partial u}{\partial x}+\frac{\partial v}{\partial y}=0 \quad (18)$$

respectively, where $Re=\nu_0/UL$ denotes the Reynolds number, $We=\lambda_1(U/L)$ is the Weissenberg number, $Fr=U/\sqrt{Lg}$ is the Froude number and $De=\lambda_2/\lambda_1$ is the Deborah number.

3. Boundary Conditions

In order to solve (13)–(18) one needs to impose boundary conditions for $\mathbf{u}$ and $\mathbf{S}$. For the momentum equations it is sufficient that we have

$$\mathbf{u} = \mathbf{0}$$

on rigid boundaries. We also have the following inflow boundary conditions for the velocity

$$u_n = U \qquad \text{and} \qquad u_\tau = 0$$

where n and τ denote the normal and tangential directions to the inflow, respectively.

3.1 Computation of the stress on rigid boundaries.

As rigid boundaries may be regarded as characteristics, the stresses S^{xx}, S^{yy} and S^{xy} on the boundary may be computed from (13)–(15), which we assume to hold on rigid boundaries with the initial condition

$$\mathbf{S} = \mathbf{0}.$$

Firstly, let us introduce the change of variables:

$$\mathbf{S} = e^{-\frac{1}{We}t}\tilde{\mathbf{S}} \tag{19}$$

By introducing (19) into (13)–(15) we obtain

$$\left(\frac{\partial \tilde{S}^{xx}}{\partial t} + u\frac{\partial \tilde{S}^{xx}}{\partial x} + v\frac{\partial \tilde{S}^{xx}}{\partial y} - 2\frac{\partial u}{\partial x}\tilde{S}^{xx} - 2\frac{\partial u}{\partial y}\tilde{S}^{xy}\right) = \frac{2}{We}\left(1 - \frac{\lambda_2}{\lambda_1}\right)e^{\frac{1}{We}t}\frac{\partial u}{\partial x} \tag{20}$$

$$\left(\frac{\partial \tilde{S}^{yy}}{\partial t} + u\frac{\partial \tilde{S}^{yy}}{\partial x} + v\frac{\partial \tilde{S}^{yy}}{\partial y} - 2\frac{\partial v}{\partial x}\tilde{S}^{xy} - 2\frac{\partial v}{\partial y}\tilde{S}^{yy}\right) = \frac{2}{We}\left(1 - \frac{\lambda_2}{\lambda_1}\right)e^{\frac{1}{We}t}\frac{\partial v}{\partial y} \tag{21}$$

$$\left(\frac{\partial \tilde{S}^{xy}}{\partial t} + u\frac{\partial \tilde{S}^{xy}}{\partial x} + v\frac{\partial \tilde{S}^{xy}}{\partial y} - \frac{\partial v}{\partial x}\tilde{S}^{xx} - \frac{\partial u}{\partial y}\tilde{S}^{yy}\right) = \frac{1}{We}\left(1 - \frac{\lambda_2}{\lambda_1}\right)e^{\frac{1}{We}t}\left(\frac{\partial u}{\partial y} + \frac{\partial v}{\partial x}\right) \tag{22}$$

- **Rigid boundary parallel to the x-axis.**

  In this case we have:

  $$u = 0, \quad v = 0 \text{ which imply } \frac{\partial u}{\partial x} = 0, \frac{\partial v}{\partial x} = 0, \text{ and so } \frac{\partial v}{\partial y} = 0$$

  from the mass conservation equation (18). In this case, the stress equations (20)–(22) reduce to:

$$\frac{\partial \tilde{S}^{xx}}{\partial t} - 2\frac{\partial u}{\partial y}\tilde{S}^{xy} = 0 \tag{23}$$

$$\frac{\partial \tilde{S}^{yy}}{\partial t} = 0 \tag{24}$$

$$\frac{\partial \tilde{S}^{xy}}{\partial t} - \frac{\partial u}{\partial y}\tilde{S}^{yy} = \frac{1}{We}\left(1 - \frac{\lambda_2}{\lambda_1}\right)e^{\frac{1}{We}t}\frac{\partial u}{\partial y} \tag{25}$$

Now, eqs. (23)–(25) may be solved for the components $\tilde{S}^{xx}$, $\tilde{S}^{yy}$ and $\tilde{S}^{xy}$. For example, from (24) with $\mathbf{S} = \mathbf{0}$ initially we get

$$\tilde{S}^{yy} = 0 \tag{26}$$

In this case, (25) reduces to

$$\frac{\partial \tilde{S}^{xy}}{\partial t} = \frac{1}{We}\left(1 - \frac{\lambda_2}{\lambda_1}\right) e^{\frac{1}{We}t} \frac{\partial u}{\partial y}$$

which gives on integration over the interval $[t\ ,\ t + \delta t]$

$$\tilde{S}^{xy}(x, y, t + \delta t) - \tilde{S}^{xy}(x, y, t) = \frac{1}{We}\left(1 - \frac{\lambda_2}{\lambda_1}\right) \int_t^{t+\delta t} \frac{\partial u(x, y, s)}{\partial y} e^{\frac{1}{We}s} ds\ . \tag{27}$$

We may write (after making use of the *mean value theorem for integrals*)

$$\tilde{S}^{xy}(x, y, t + \delta t) - \tilde{S}^{xy}(x, y, t) = \frac{1}{We}\left(1 - \frac{\lambda_2}{\lambda_1}\right) \frac{\partial u(x, y, t^*)}{\partial y} \int_t^{t+\delta t} e^{\frac{1}{We}s} ds \tag{28}$$

where $\frac{\partial u}{\partial y}$ takes the value at some $t^* \in (t, t + \delta t)$, giving

$$\tilde{S}^{xy}(x, y, t + \delta t) = \tilde{S}^{xy}(x, y, t) + \left(1 - \frac{\lambda_2}{\lambda_1}\right) \frac{\partial u(x, y, t^*)}{\partial y} e^{\frac{1}{We}t} \left[e^{\frac{1}{We}\delta t} - 1\right]\ . \tag{29}$$

Thus, on rigid boundaries parallel to the x-axis, S^{xy} is given by

$$\begin{aligned} S^{xy}(x, y, t + \delta t) &= e^{-\frac{1}{We}(t+\delta t)} \tilde{S}^{xy}(x, y, t + \delta t) \\ &= e^{-\frac{1}{We}(t+\delta t)} \left\{ \tilde{S}^{xy}(x, y, t) + \left(1 - \frac{\lambda_2}{\lambda_1}\right) \frac{\partial u}{\partial y}(x, y, t^*) e^{\frac{1}{We}t} \left[e^{\frac{1}{We}\delta t} - 1\right] \right\} \\ &= e^{-\frac{1}{We}\delta t} S^{xy}(x, y, t) + \left(1 - \frac{\lambda_2}{\lambda_1}\right) \frac{\partial u}{\partial y}(x, y, t^*) \left[1 - e^{-\frac{1}{We}\delta t}\right]\ . \end{aligned} \tag{30}$$

To calculate S^{xx} we integrate (23) over $[t,\ t + \delta t]$ to obtain

$$\tilde{S}^{xx}(x, y, t + \delta t) = \tilde{S}^{xx}(x, y, t) + 2 \int_t^{t+\delta t} \frac{\partial u(x, y, s)}{\partial y} \tilde{S}^{xy}(x, y, s) ds\ . \tag{31}$$

Approximating

$$\int_t^{t+\delta t} \frac{\partial u(x, y, s)}{\partial y} \tilde{S}^{xy}(x, y, s) ds$$

by the trapezoidal rule, yields

$$\tilde{S}^{xx}(x, y, t+\delta t) = \tilde{S}^{xx}(x, y, t) + \delta t \left[\frac{\partial u}{\partial y}(x, y, t) \tilde{S}^{xy}(x, y, t) + \frac{\partial u}{\partial y}(x, y, t + \delta t) \tilde{S}^{xy}(x, y, t + \delta t)\right] \tag{32}$$

Finally, multiplying (32) by the factor $e^{-\frac{1}{We}(t+\delta t)}$ we obtain

$$S^{xx}(x,y,t+\delta t) = e^{-\frac{1}{We}\delta t}S^{xx}(x,y,t) + \delta t\left[\frac{\partial u}{\partial y}(x,y,t)e^{-\frac{1}{We}\delta t}S^{xy}(x,y,t) + \frac{\partial u}{\partial y}(x,y,t+\delta t)S^{xy}(x,y,t+\delta t)\right] \quad (33)$$

- **Rigid boundary parallel to the y-axis.** Here we have

$$u = 0, \quad v = 0 \text{ which implies that } \frac{\partial u}{\partial y} = 0, \frac{\partial v}{\partial y} = 0 \text{ and so } \frac{\partial u}{\partial x} = 0$$

from the continuity equation (18). Introducing these values into (20)–(22) yields

$$\frac{\partial \tilde{S}^{xx}}{\partial t} = 0 \quad (34)$$

$$\frac{\partial \tilde{S}^{yy}}{\partial t} - 2\frac{\partial v}{\partial x}\tilde{S}^{xy} = 0 \quad (35)$$

$$\frac{\partial \tilde{S}^{xy}}{\partial t} - \frac{\partial v}{\partial x}\tilde{S}^{xx} = \frac{1}{We}\left(1 - \frac{\lambda_2}{\lambda_1}\right)e^{\frac{1}{We}t}\frac{\partial v}{\partial x} \quad (36)$$

Likewise the derivation of S^{xx}, S^{xy} and S^{yy} on rigid boundaries parallel to the x-axis gives

$$S^{xx}(x,y,t) = 0 \quad (37)$$

$$S^{xy}(x,y,t+\delta t) = e^{-\frac{1}{We}\delta t}S^{xy}(x,y,t) + \left(1 - \frac{\lambda_2}{\lambda_1}\right)\frac{\partial v}{\partial x}(x,y,t^*)\left[1 - e^{-\frac{1}{We}\delta t}\right]. \quad (38)$$

$$S^{yy}(x,y,t+\delta t) = e^{-\frac{1}{We}\delta t}S^{yy}(x,y,t) + \delta t\left[\frac{\partial v}{\partial x}(x,y,t)e^{-\frac{1}{We}\delta t}S^{xy}(x,y,t) + \frac{\partial v}{\partial x}(x,y,t+\delta t)S^{xy}(x,y,t+\delta t)\right] \quad (39)$$

3.2 Inflow and Outflow boundaries

These can be specified as follows:

- **Inflow boundary**: At the fluid entrance we impose the velocity components

$$u_n = U \qquad \text{and} \qquad u_\tau = 0$$

while for the non-Newtonian extra stress tensor components $\mathbf{S}$ we adopt the strategy of Crochet et al. [2] and Mompean and Deville [3], namely:

$$S^{xx} = 0, \qquad S^{xy} = 0 \quad \text{and} \quad S^{yy} = 0. \tag{40}$$

- **Outflow boundary**: At fluid exit we impose homegeneous Neumann conditions for both the velocity components and the extra stress components, namely

$$\frac{\partial u_n}{\partial n} = 0, \qquad \frac{\partial u_\tau}{\partial n} = 0$$

$$\frac{\partial S^{xx}}{\partial n} = \frac{\partial S^{xy}}{\partial n} = \frac{\partial S^{yy}}{\partial n} = 0. \tag{41}$$

In the equations above the subscripts n and τ denote directions normal and tangential to the boundary, respectively.

3.3 Free Surface Stress Conditions

We shall consider unsteady free-surface flows of viscous fluid moving into a passive atmosphere (which we may take to be at zero pressure). In the absence of surface tension the normal and tangential components of stress must be continuous across any free surface, so that on such a surface (see Batchelor [27])

$$\mathbf{n} \cdot (\sigma \cdot \mathbf{n}) = 0 \qquad \text{and} \qquad \mathbf{m} \cdot (\sigma \cdot \mathbf{n}) = 0 \tag{42}$$

where $\sigma = \sigma_{ij}$ is the stress tensor given by:

$$\sigma_{ij} = -p\delta_{ij} + T_{ij}, \qquad i, j = 1, 2$$

and T_{ij} is given by (4). The finite difference equations approximating these conditions are given in Section 4.2.

4. Method of Solution

To solve equations (13)–(18) we employ a procedure similar to that introduced by Tomé et al. [25] for a generalized Newtonian fluid.

Let us suppose that at a given time, say t_n, the velocity field $\mathbf{u}(\mathbf{x}, t_n)$ and the non-Newtonian extra stress tensor $\mathbf{S}(\mathbf{x}, t_n)$ are known and boundary conditions for the $\mathbf{u}$ and $\mathbf{S}$ and pressure are given. To compute the velocity field, pressure field and the non-Newtonian extra-stress tensor at the advanced time $t_{n+1} = t_n + \delta t$, we proceed as follows:

Step 1: Let $\tilde{p}(\mathbf{x}, t_n)$ be a pressure field which satisfies the correct pressure condition on the free surface. This pressure field is computed from the stress conditions (42).

Step 2: Calculate the intermediate velocity field, $\tilde{\mathbf{u}}(\mathbf{x}, t_{n+1})$, from

$$\frac{\partial \tilde{u}}{\partial t} = -\frac{\partial (u^2)}{\partial x} - \frac{\partial (uv)}{\partial y} - \frac{\partial \tilde{p}}{\partial x} + \frac{1}{Re}\left(\frac{\lambda_2}{\lambda_1}\right)\left(\frac{\partial^2 u}{\partial x^2} + \frac{\partial^2 u}{\partial y^2}\right) + \frac{1}{Re}\left(\frac{\partial S^{xx}}{\partial x} + \frac{\partial S^{xy}}{\partial y}\right) + \frac{1}{F_r^2} g_x \quad (43)$$

$$\frac{\partial \tilde{v}}{\partial t} = -\frac{\partial (uv)}{\partial x} - \frac{\partial (v^2)}{\partial y} - \frac{\partial \tilde{p}}{\partial y} + \frac{1}{Re}\left(\frac{\lambda_2}{\lambda_1}\right)\left(\frac{\partial^2 v}{\partial x^2} + \frac{\partial^2 v}{\partial y^2}\right) + \frac{1}{Re}\left(\frac{\partial S^{xy}}{\partial x} + \frac{\partial S^{yy}}{\partial y}\right) + \frac{1}{F_r^2} g_y \quad (44)$$

with $\tilde{\mathbf{u}}(\mathbf{x}, t_n) = \mathbf{u}(\mathbf{x}, t_n)$ using the correct boundary conditions for $\mathbf{u}(\mathbf{x}, t_n)$. These equations are solved by a finite difference method which is usually, but not necessarily, explicit.

Step 3: Solve the Poisson equation

$$\nabla^2 \psi(\mathbf{x}, t_{n+1}) = \nabla . \tilde{\mathbf{u}}(\mathbf{x}, t_{n+1}). \quad (45)$$

The appropriate boundary conditions for this equation are (see Tomé et al. [25])

$$\frac{\partial \psi}{\partial n} = 0 \qquad \text{on rigid boundaries and} \qquad \psi = 0 \qquad \text{on the free surface.}$$

Step 4: Compute the velocity field

$$\mathbf{u}(\mathbf{x}, t_{n+1}) = \tilde{\mathbf{u}}(\mathbf{x}, t_{n+1}) - \nabla \psi(\mathbf{x}, t_{n+1}). \quad (46)$$

Step 5: Compute the pressure

$$p(\mathbf{x}, t_{n+1}) = \tilde{p}(\mathbf{x}, t_n) + \frac{\psi(\mathbf{x}, t_{n+1})}{\delta t}. \quad (47)$$

Step 6: Update the components of the non-Newtonian extra-stress tensor on rigid boundaries according to the equations given in Section 2.1

Step 7: Compute the components of the non-Newtonian extra-stress tensor, $S^{xx}(\mathbf{x}, t_{n+1})$, $S^{xy}(\mathbf{x}, t_{n+1})$, $S^{yy}(\mathbf{x}, t_{n+1})$, from:

$$\frac{\partial S^{xx}}{\partial t} = \left[-\frac{\partial (uS^{xx})}{\partial x} - \frac{\partial (vS^{xx})}{\partial y} + 2\frac{\partial u}{\partial x} S^{xx} + 2\frac{\partial u}{\partial y} S^{xy} + \frac{1}{We}\left[2\left(1 - \frac{\lambda_2}{\lambda_1}\right)\frac{\partial u}{\partial x} - S^{xx} \right] \right]_{t_n} \quad (48)$$

$$\frac{\partial S^{yy}}{\partial t} = \left[-\frac{\partial (uS^{yy})}{\partial x} - \frac{\partial (vS^{yy})}{\partial y} + 2\frac{\partial v}{\partial x} S^{xy} + 2\frac{\partial v}{\partial y} S^{yy} + \frac{1}{We}\left[2\left(1 - \frac{\lambda_2}{\lambda_1}\right)\frac{\partial v}{\partial y} - S^{yy} \right] \right]_{t_n} \quad (49)$$

$$\frac{\partial S^{xy}}{\partial t} = \left[-\frac{\partial (uS^{xy})}{\partial x} - \frac{\partial (vS^{xy})}{\partial y} + \frac{\partial v}{\partial x} S^{xx} + \frac{\partial u}{\partial y} S^{yy} + \frac{1}{We}\left[\left(1 - \frac{\lambda_2}{\lambda_1}\right)\left(\frac{\partial u}{\partial y} + \frac{\partial v}{\partial x}\right) - S^{xy} \right] \right]_{t_n} \quad (50)$$

Equations (48)–(50) are solved by finite differences. Details of the difference equations are given in the next Section.

Step 8: Update the markers positions: The last step in the calculation is to move the markers to their new positions. This is done by solving

$$\frac{dx}{dt} = u \ , \qquad \frac{dy}{dt} = v \ , \quad (51)$$

for each particle. The fluid surface is defined by a list containing these markers and the visualization of the free surface is obtained simply by connecting them by straight lines.

5. Basic Finite Difference Equations

Equations (43)–(50) will be solved by finite differences. A staggered grid is employed and typical cell is displayed in figure 1.

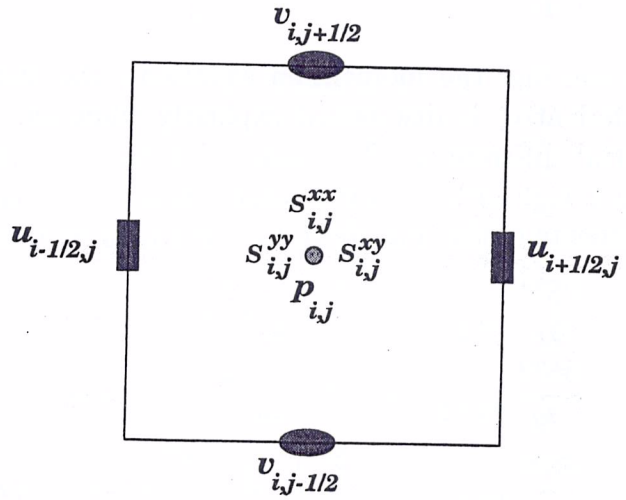

Fig. 1. Typical cell for an Oldroyd-B fluid flow calculation.

The components of the non-Newtonian extra-stress tensor (48)–(50) are applied at the centre of a cell. They are approximated by finite differences as follows: the time derivative is approximated by an explicit discretization while the spatial derivatives are approximated by central differences. The convective terms are approximated by a high order bounded upwind scheme employing the VONOS method [28]. Details of the implementation of this high order bounded upwinding scheme can be found in [29] where it was employed to simulate a Newtonian hydraulic jump. Thus, equations (48)–(50) are approximated by

$$S^{xx(n+1)}_{i,j} = \left(1 - \frac{\delta t}{We}\right) S^{xx}_{i,j} - \delta t \left[\mathbf{conv}(uS^{xx})_{i,j} + \mathbf{conv}(vS^{xx})_{i,j} - 2\frac{(u_{i+\frac{1}{2},j} - u_{i-\frac{1}{2},j})}{\delta x} S^{xx}_{i,j} \right.$$
$$\left. -2\frac{(u_{i,j+\frac{1}{2}} - u_{i,j-\frac{1}{2}})}{\delta y} S^{xy}_{i,j} + \frac{2}{We}\left(\frac{\lambda_2}{\lambda_1} - 1\right)\frac{(u_{i+\frac{1}{2},j} - u_{i-\frac{1}{2},j})}{\delta x}\right], \tag{52}$$

$$S^{yy(n+1)}_{i,j} = (1 - \frac{\delta t}{We})S^{yy}_{i,j} - \delta t \left[\mathbf{conv}(uS^{yy})_{i,j} + \mathbf{conv}(vS^{yy})_{i,j} - 2\frac{(v_{i,j+\frac{1}{2}} - v_{i,j-\frac{1}{2}})}{\delta y} S^{yy}_{i,j} \right.$$
$$\left. -2\frac{(v_{i+\frac{1}{2},j} - v_{i-\frac{1}{2},j})}{\delta x} S^{xy}_{i,j} + \frac{2}{We}\left(\frac{\lambda_2}{\lambda_1} - 1\right)\frac{(v_{i,j+\frac{1}{2}} - v_{i,j-\frac{1}{2}})}{\delta y}\right], \tag{53}$$

$$S^{xy(n+1)}_{i,j} = (1 - \frac{\delta t}{We})S^{xy}_{i,j} - \delta t \left[\mathbf{conv}(uS^{xy})_{i,j} + \mathbf{conv}(vS^{xy})_{i,j} - \frac{(v_{i+\frac{1}{2},j} - v_{i-\frac{1}{2},j})}{\delta x} S^{xx}_{i,j} \right.$$
$$\left. -\frac{(u_{i,j+\frac{1}{2}} - u_{i,j-\frac{1}{2}})}{\delta y} S^{yy}_{i,j} + \frac{1}{We}\left(\frac{\lambda_2}{\lambda_1} - 1\right)\left(\frac{u_{i,j+\frac{1}{2}} - u_{i,j-\frac{1}{2}}}{\delta y} + \frac{v_{i+\frac{1}{2},j} - v_{i-\frac{1}{2},j}}{\delta x}\right)\right]. \tag{54}$$

In equations (52)–(54), terms which are not defined at cell position are obtained by averaging, that is:

$$u_{i,j+\frac{1}{2}} := \frac{u_{i+\frac{1}{2},j} + u_{i+\frac{1}{2},j+1} + u_{i-\frac{1}{2},j} + u_{i-\frac{1}{2},j+1}}{4},$$
$$v_{i+\frac{1}{2},j} := \frac{v_{i,j+\frac{1}{2}} + v_{i+1,j+\frac{1}{2}} + v_{i,j-\frac{1}{2}} + v_{i+1,j-\frac{1}{2}}}{4}.$$

For instance, if we consider the momentum equations, the discretization is performed as follows: the time derivative is discretized explicitly while the spatial derivatives are approximated by central differences. The convective terms of (43) and (44), $\mathbf{conv}(\cdot)$, are approximated using a high order upwind scheme using the Vonos scheme [28]. The terms involving the components of the non-Newtonian extra-stress tensor are approximated by

$$\begin{aligned}
\frac{\partial S^{xx}}{\partial x}\Big|_{i+\frac{1}{2},j} &= \frac{S^{xx}_{i+1,j} - S^{xx}_{i,j}}{\delta x} + O(\delta x^2) \\
\frac{\partial S^{yy}}{\partial y}\Big|_{i,j+\frac{1}{2}} &= \frac{S^{yy}_{i,j+1} - S^{yy}_{i,j}}{\delta y} + O(\delta y^2) \\
\frac{\partial S^{xy}}{\partial y}\Big|_{i+\frac{1}{2},j} &= \frac{S^{xy}_{i+\frac{1}{2},j+\frac{1}{2}} - S^{xy}_{i+\frac{1}{2},j-\frac{1}{2}}}{\delta y} + O(\delta y^2)
\end{aligned}$$

where terms like $S^{xy}_{i+\frac{1}{2},j+\frac{1}{2}}$ are obtained by averaging the four nearest values, e.g.

$$S^{xy}_{i+\frac{1}{2},j+\frac{1}{2}} := 0.25 * (S^{xy}_{i,j} + S^{xy}_{i+1,j} + S^{xy}_{i,j+1} + S^{xy}_{i+1,j+1}) \tag{55}$$

Thus, equations (43) and (44) are approximated by

$$\begin{aligned}
\tilde{u}_{i+\frac{1}{2},j} = u_{i+\frac{1}{2},j} - \delta t \Bigg[& \mathbf{conv}(u^2) + \mathbf{conv}(uv) + \frac{\tilde{p}_{i+1,j} - \tilde{p}_{i,j}}{\delta x} \\
& + \frac{1}{Re}\left(\frac{\lambda_2}{\lambda_1}\right)\left(\frac{u_{i-\frac{1}{2},j} - 2u_{i+\frac{1}{2},j} + u_{i+\frac{3}{2},j}}{\delta x^2} + \frac{u_{i+\frac{1}{2},j-1} - 2u_{i+\frac{1}{2},j} + u_{i+\frac{1}{2},j+1}}{\delta y^2}\right) \\
& - \frac{1}{Re}\left(\frac{S^{xx}_{i+1,j} - S^{xx}_{i,j}}{\delta x} + \frac{S^{xy}_{i+\frac{1}{2},j+\frac{1}{2}} - S^{xy}_{i+\frac{1}{2},j-\frac{1}{2}}}{\delta y}\right) - \frac{1}{Fr^2} g_x \Bigg]
\end{aligned} \tag{56}$$

and

$$\begin{aligned}
\tilde{v}_{i,j+\frac{1}{2}} = v_{i,j+\frac{1}{2}} - \delta t \Bigg[& \mathbf{conv}(vu) + \mathbf{conv}(v^2) + \frac{\tilde{p}_{i,j+1} - \tilde{p}_{i,j}}{\delta y} + \\
& + \frac{1}{Re}\left(\frac{\lambda_2}{\lambda_1}\right)\left(\frac{v_{i-1,j+\frac{1}{2}} - 2v_{i,j+\frac{1}{2}} + v_{i+1,j+\frac{1}{2}}}{\delta x^2} + \frac{v_{i,j-\frac{1}{2}} - 2v_{i,j+\frac{1}{2}} + v_{i,j+\frac{3}{2}}}{\delta y^2}\right) \\
& - \frac{1}{Re}\left(\frac{S^{xy}_{i+\frac{1}{2},j+\frac{1}{2}} - S^{xy}_{i-\frac{1}{2},j+\frac{1}{2}}}{\delta x} + \frac{S^{yy}_{i,j+1} - S^{yy}_{i,j}}{\delta y}\right) - \frac{1}{Fr^2} g_y \Bigg].
\end{aligned} \tag{57}$$

The Poisson equation (45) is discretized at cell centres using the five-point Laplacian, namely,

$$\frac{\psi_{i+1,j} - 2\psi_{i,j} + \psi_{i-1,j}}{\delta x^2} + \frac{\psi_{i,j+1} - 2\psi_{i,j} + \psi_{i,j-1}}{\delta y^2} = \tilde{D}_{i,j} \tag{58}$$

where

$$\tilde{D}_{i,j} = \frac{\tilde{u}_{i+\frac{1}{2},j} - \tilde{u}_{i-\frac{1}{2},j}}{\delta x} + \frac{\tilde{v}_{i,j+\frac{1}{2}} - \tilde{v}_{i,j-\frac{1}{2}}}{\delta y} .$$

Equation (58) leads to a symmetric and positive definite linear system for $\psi_{i,j}$. In order to solve this linear system we employ the conjugate gradient method as implemented in GENSMAC (see Tomé and McKee [12]). The final velocities are obtained by discretizing (46) at the respective nodes, namely

$$\begin{cases} u^{n+1}_{i+\frac{1}{2},j} = \tilde{u}_{i+\frac{1}{2},j} - \left(\dfrac{\psi_{i+1,j} - \psi_{i,j}}{\delta x} \right), \\ v^{n+1}_{i,j+\frac{1}{2}} = \tilde{v}_{i,j+\frac{1}{2}} - \left(\dfrac{\psi_{i,j+1} - \psi_{i,j}}{\delta y} \right). \end{cases} \tag{59}$$

The pressure is obtained by applying (47) at the cell centres, giving

$$p_{i,j} = \tilde{p}_{i,j} + \frac{\psi_{i,j}}{\delta t} \tag{60}$$

Consequently, each calculational cycle consists of solving equations (52)–(60) at each time-step.

5.1 Cell Flagging

As the fluid is continuously moving, a procedure for identifying the fluid region and the free surface is employed. To effect this, the cells within the mesh are flagged as:

- Empty (E) - Cells that do not contain fluid
- Full (F) - Cells full of fluid. These cells do not have any face contiguous with an Empty cell.
- Surface (S) - Cells that contain fluid and have at least one face contiguous with an Empty cell face. These cells contain the free surface.
- Boundary (B) - Cells that define a rigid boundary. In these cells the no-slip condition is applied.

- Inflow (I) - Cells that define an inflow boundary.

Figure 2 illustrates the cell structure for a two–dimensional flow at a given instant of time. For clarity, the empty cells are left blank.

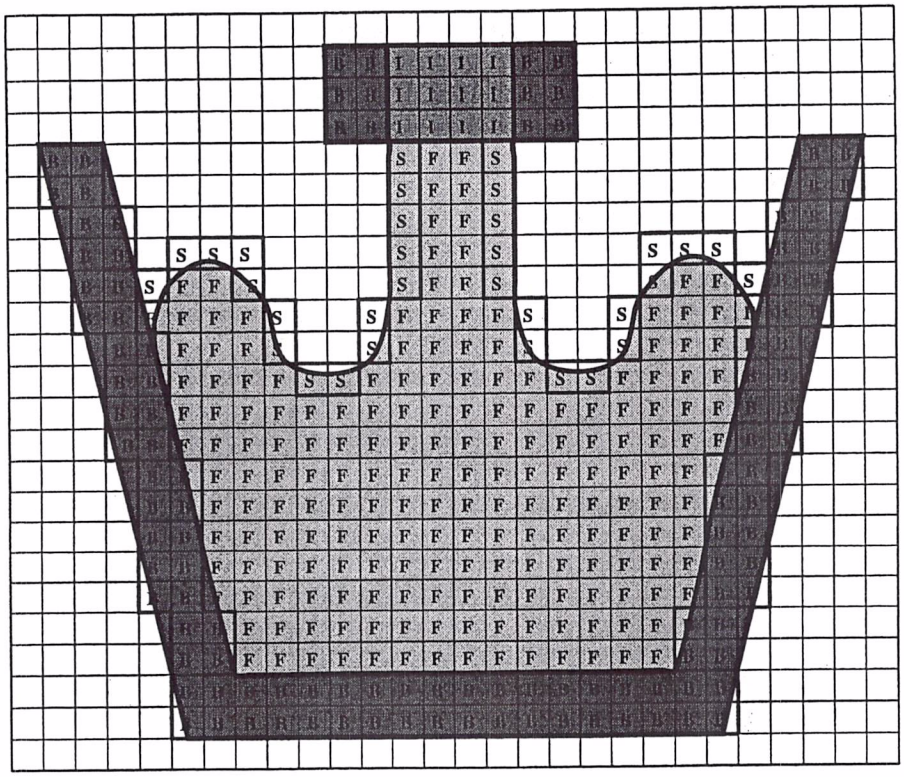

Fig. 2. Types of cells used in a GENSMAC calculation.

5.2 Free Surface Stress Conditions

By using two-dimensional cartesian coordinates, the stress conditions (42) can be written as

$$p - \frac{1}{Re}\left[2\frac{\lambda_2}{\lambda_1}\left(\frac{\partial u}{\partial x}n_x^2 + \left(\frac{\partial u}{\partial y} + \frac{\partial v}{\partial x}\right)n_x n_y + \frac{\partial v}{\partial y}n_y^2\right) + S^{xx}n_x^2 + S^{xy}n_x n_y + S^{yy}n_y^2\right] = 0, \quad (61)$$

$$\frac{1}{Re}\left[\frac{\lambda_2}{\lambda_1}\left(2\left(\frac{\partial v}{\partial y} - \frac{\partial u}{\partial x}\right)n_x n_y + \left(\frac{\partial u}{\partial y} + \frac{\partial v}{\partial x}\right)(n_x^2 - n_y^2)\right)\right.$$
$$\left. + \left(S^{yy} - S^{xx}\right)n_x n_y + S^{xy}\left(n_x^2 - n_y^2\right)\right] = 0. \quad (62)$$

Equations (61)–(62) represent the appropriate boundary condition on a free surface (see Batchelor, page 153 [27]). To apply these conditions we proceed as follows:

Let us assume that the mesh spacing is sufficiently small so that the free surface will intercept a mesh cell at two edges. Then conditions (61)–(62) can be applied according to three cases:

(i) **Surface cell (S) having only one face contiguous with an empty cell (E)**: In these cells it is assumed that the free surface is either horizontal or vertical according to which side is contiguous with the empty cell. In this case the normal vector takes the form $\mathbf{n} = (n_x, 0)$ or $\mathbf{n} = (0, n_y)$.

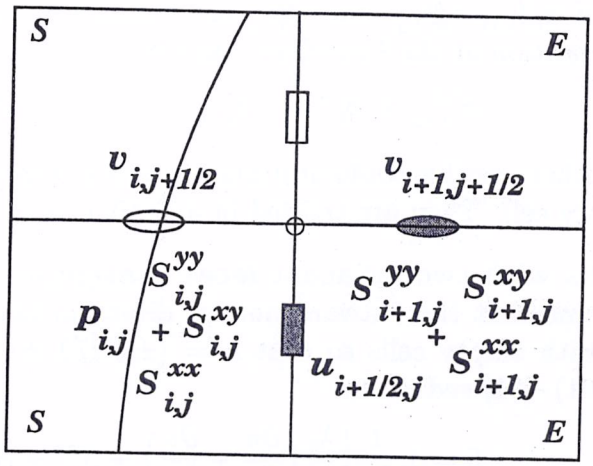

Fig. 8. Surface cell having only the right side contiguous with an empty cell.

For instance, if we consider the surface cell shown in figure 8 we take $\mathbf{n} = (1, 0)$. In this case the stress conditions (61)–(62) reduce to

$$\tilde{p} - \frac{1}{Re}\left[\frac{\lambda_2}{\lambda_1}\left(2\frac{\partial u}{\partial x}\right) + S^{xx}\right] = 0, \tag{63}$$

$$\frac{\lambda_2}{\lambda_1}\left(\frac{\partial u}{\partial y} + \frac{\partial v}{\partial x}\right) + S^{xy} = 0. \tag{64}$$

We observe that when computing the tilde velocities using (56)–(57), the values of $\tilde{p}_{i,j}$, $u_{i+\frac{1}{2},j}$, $v_{i+1,j+\frac{1}{2}}$ and the extra-stress components $S^{xx}_{i,j}, S^{yy}_{i,j}, S^{xx}_{i+1,j}, S^{yy}_{i+1,j}$, and $S^{xy}_{i+1,j}$ are required. They can be obtained as follows:

Firstly, discretizing the continuity equation (18) at the cell centre we obtain

$$u_{i+\frac{1}{2},j} = u_{i-\frac{1}{2},j} - \frac{\delta_x}{\delta y}\left(v_{i,j+\frac{1}{2}} - v_{i,j-\frac{1}{2}}\right).$$

Now, applying condition (64) at cell corner $(i+\frac{1}{2}, j+\frac{1}{2})$ we get

$$\frac{\lambda_2}{\lambda_1}\left(\frac{u_{i+\frac{1}{2},j+1}-u_{i+\frac{1}{2},j}}{\delta y}+\frac{v_{i+1,j+\frac{1}{2}}-v_{i,j+\frac{1}{2}}}{\delta x}\right)+S^{xy}_{i+\frac{1}{2},j+\frac{1}{2}}=0$$

which yields

$$v_{i+1,j+\frac{1}{2}}=v_{i,j+\frac{1}{2}}-\frac{\delta x}{\delta y}\left(u_{i+\frac{1}{2},j+1}-u_{i+\frac{1}{2},j}\right)-\delta x\frac{\lambda_1}{\lambda_2}S^{xy}_{i+\frac{1}{2},j+\frac{1}{2}}.$$

The value of $S^{xy}_{i+\frac{1}{2},j+\frac{1}{2}}$ is obtained by averaging (see (55)). Having computed the velocities, the pressure $\tilde{p}_{i,j}$ follows from (63) applied at the cell centre:

$$\tilde{p}_{i,j}=\frac{1}{Re}\left[2\frac{\lambda_2}{\lambda_1}\left(\frac{u_{i+\frac{1}{2},j}-u_{i-\frac{1}{2},j}}{\delta r}\right)+S^{xx}_{i,j}\right].$$

The values of $S^{xy}_{i+1,j}$, $S^{xx}_{i+1,j}$ and $S^{yy}_{i+1,j}$ are obtained by assuming that they satisfy the Neumann condition at the boundary, namely

$$S^{xy}_{i+1,j}=S^{xy}_{i,j}\qquad S^{xx}_{i+1,j}=S^{xx}_{i,j}\qquad S^{yy}_{i+1,j}=S^{yy}_{i,j}$$

There are 3 other possible configurations of surface cells having only one face contiguous with an empty cell. They are treated in a similar manner.

(ii) **Surface cells with two adjacent faces contiguous with empty cells**: For these cells we assume that the outward normal direction lies at 45^o between the two faces contiguous with empty cells so that $\mathbf{n}=(\pm\sqrt{2}/2, \pm\sqrt{2}/2)$. In this case, the stress conditions (61)–(62) reduce to

$$\tilde{p}=\pm\frac{1}{Re}\left[\frac{\lambda_2}{\lambda_1}\left(\frac{\partial u}{\partial y}+\frac{\partial v}{\partial x}\right)+S^{xx}+S^{xy}+S^{yy}\right], \tag{65}$$

$$2\frac{\lambda_2}{\lambda_1}\left(\frac{\partial v}{\partial y}-\frac{\partial u}{\partial x}\right)+S^{yy}-S^{xx}=0, \tag{66}$$

respectively. The sign in (65) is chosen according to which sides are contiguous with the empty cells.

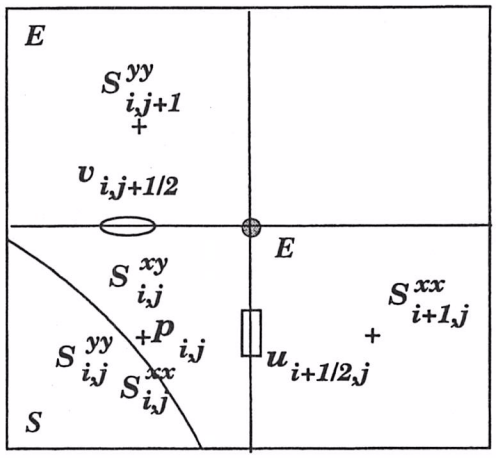

Fig. 9. Surface cell with the right and top sides contiguous with empty cells.

For instance, by considering figure 9, we observe that the values of $\widetilde{p}_{i,j}$, $u_{i+\frac{1}{2},j}$, $v_{i,j+\frac{1}{2}}$, $S^{xx}_{i+1,j}$, $S^{yy}_{i+1,j}$, $S^{xy}_{i+1,j}$, $S^{xx}_{i,j+1}$, $S^{yy}_{i,j+1}$ and $S^{xy}_{i,j+1}$ are necessary when computing the tilde velocities and the extra stress components. They are obtained from the conditions $\partial S/\partial x = 0$ and $\partial S/\partial y = 0$ which we have assumed to hold. In this case we get

$$S^{xx}_{i+1,j} = S^{xx}_{i,j}, \qquad S^{yy}_{i+1,j} = S^{yy}_{i,j}, \qquad S^{xy}_{i+1,j} = S^{xx}_{i,j}$$

$$S^{xx}_{i,j+1} = S^{xx}_{i,j} \qquad S^{yy}_{i,j+1} = S^{yy}_{i,j}, \qquad S^{xy}_{i,j+1} = S^{xx}_{i,j}.$$

Now, in order to compute $u_{i+\frac{1}{2},j}$ and $v_{i,j+\frac{1}{2}}$, the continuity equation (18) and the tangential stress condition (66) are used which, when discretized at a cell centre, produce

$$\frac{u_{i+\frac{1}{2},j} - u_{i-\frac{1}{2},j}}{\delta x} + \frac{v_{i,j+\frac{1}{2}} - v_{i,j-\frac{1}{2}}}{\delta y} = 0 \tag{67}$$

$$2\frac{\lambda_2}{\lambda_1}\left(\frac{v_{i,j+\frac{1}{2}} - v_{i,j-\frac{1}{2}}}{\delta y} - \frac{u_{i+\frac{1}{2},j} - u_{i-\frac{1}{2},j}}{\delta x}\right) + S^{yy}_{i,j} - S^{xx}_{i,j} = 0. \tag{68}$$

Equations (67) and (68) give now a 2×2 linear system for $u_{i+\frac{1}{2},j}$ and $v_{i,j+\frac{1}{2}}$, yielding

$$u_{i+\frac{1}{2},j} = u_{i-\frac{1}{2},j} - \frac{\delta_x}{4}\frac{\lambda_1}{\lambda_2}\left(S^{xx}_{i,j} - S^{yy}_{i,j}\right); \qquad v_{i,j+\frac{1}{2}} = v_{i,j-\frac{1}{2}} + \frac{\delta y}{4}\frac{\lambda_1}{\lambda_2}\left(S^{xx}_{i,j} - S^{yy}_{i,j}\right). \tag{69}$$

Having computed $u_{i+\frac{1}{2},j}$ and $v_{i,j+\frac{1}{2}}$, the pressure at the cell centre follows from (65) giving

$$\begin{aligned}\widetilde{p}_{i,j} = \frac{1}{Re}\Bigg[\frac{\lambda_2}{\lambda_1}\Bigg(&\frac{u_{i+\frac{1}{2},j} + u_{i-\frac{1}{2},j} - u_{i+\frac{1}{2},j-1} - u_{i-\frac{1}{2},j-1}}{\delta z} \\ &+ \frac{v_{i,j+\frac{1}{2}} + v_{i,j-\frac{1}{2}} - v_{i-1,j+\frac{1}{2}} - v_{i-1,j-\frac{1}{2}}}{\delta r}\Bigg) \\ &+ S^{xx}_{i,j} + S^{yy}_{i,j} + S^{xy}_{i,j}\Bigg].\end{aligned}$$

The remaining configurations of surface cells having only two faces contiguous with empty cells are handled similarly.

(iii) **Surface cells having two opposite sides contiguous with empty cells**: For these cells we cannot obtain an approximation for the normal vector. In these cells one velocity is adjusted so that the continuity equation is satisfied. The pressure and the extra-stress components are set to zero. If these cells appear, a finer mesh should be employed to minimize their presence.

Instituto de Ciências Matemáticas
Biblioteca
São Carlos

5.3 Computation of the non-Newtonian extra-stress components on rigid boundaries

When the discretized momentum equations (56)–(57) and the extra-stress components (52)–(54) are applied on nodes that are adjacent to the boundary then the values of S^{xx}, S^{yy} and S^{xy} on the boundary cells are required. They can be obtained from the boundary conditions given in Section 3.1 The following cases are considered:

(i) **Boundary cells having only the top (or bottom) side contiguous with an interior cell:** In this case we assume that the boundary is a horizontal surface (see figure 10) and apply the equations derived in Section 3.1.

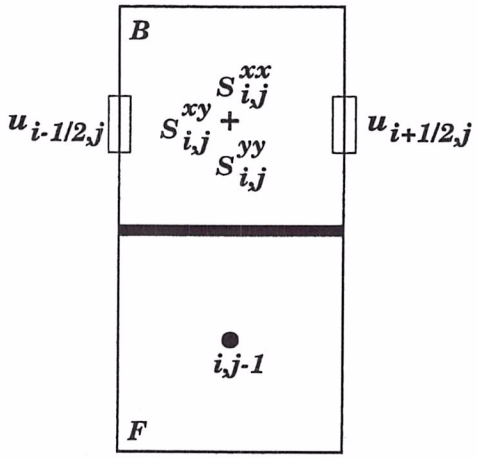

Fig. 10. Boundary cells having only the bottom side contiguous with an interior cell.

For instance, from consideration of figure 10 and from equations (26), (30) and (33), the values of the non-Newtonian extra-stress components are given by

$$S^{yy}_{i,j-\frac{1}{2}} = 0 \tag{70}$$

$$S^{xy}_{i,j-\frac{1}{2}}(t_{n+1}) = e^{-\frac{1}{We}\delta t} S^{xy}_{i,j-\frac{1}{2}}(t_n) + \left(1 - \frac{\lambda_2}{\lambda_1}\right) \frac{\partial u}{\partial y}(x_i, y_{j-\frac{1}{2}}, t^*) \left[e^{-\frac{1}{We}\delta t} - 1\right] \tag{71}$$

$$S^{xx}_{i,j-\frac{1}{2}}(t_{n+1}) = e^{-\frac{1}{We}\delta t} S^{xx}_{i,j-\frac{1}{2}}(t_n) + \delta t \frac{\partial u}{\partial y}(x_i, y_{j-\frac{1}{2}}, t^*) \left[e^{-\frac{1}{We}\delta t} S^{xy}_{i,j-\frac{1}{2}}(t_n) + S^{xy}_{i,j-\frac{1}{2}}(t_{n+1})\right] \tag{72}$$

where the value of $\frac{\partial u}{\partial y}(x_i, y_{j-\frac{1}{2}}, t^*)$ is obtained by averaging $\frac{\partial u}{\partial y}(x_i, y_{j-\frac{1}{2}}, t)$ at times t_n and t_{n+1}, namely,

$$\frac{\partial u}{\partial y}(x_i, y_{j-\frac{1}{2}}, t^*) = \frac{1}{2}\left[\frac{\partial u}{\partial y}(x_i, y_{j-\frac{1}{2}}, t_n) + \frac{\partial u}{\partial y}(x_i, y_{j-\frac{1}{2}}, t_{n+1})\right]$$

and the derivatives are approximated by

$$\frac{\partial u}{\partial y}(x_i, y_{j-\frac{1}{2}}, t_n) = \frac{u^n_{i,j} - u^n_{i,j-1}}{\delta y}, \qquad \frac{\partial u}{\partial y}(x_i, y_{j-\frac{1}{2}}, t_{n+1}) = \frac{u^{n+1}_{i,j} - u^{n+1}_{i,j-1}}{\delta y}$$

where the velocities at cell positions (i, j) and $(i, j-1)$ are given by

$$u_{i,j} = \frac{u_{i+\frac{1}{2},j} + u_{i-\frac{1}{2},j}}{2} \qquad \text{and} \qquad u_{i,j-1} = \frac{u_{i+\frac{1}{2},j-1} + u_{i-\frac{1}{2},j-1}}{2}, \text{ respectively.}$$

Finally, the values of $S^{xx}_{i,j}$ and $S^{yy}_{i,j}$ are obtained by performing linear interpolation using the nodes $(i, j-\frac{1}{2})$ and $(i, j-1)$, respectively.

(ii) Boundary cell having only the right (left) side contiguous with a interior cell: In these cells (see figure 11) we assume that the rigid boundary is parallel to the y-axis. The computation of the non-Newtonian extra-stress components is performed according to the equations derived in Section 3.1 as follows.

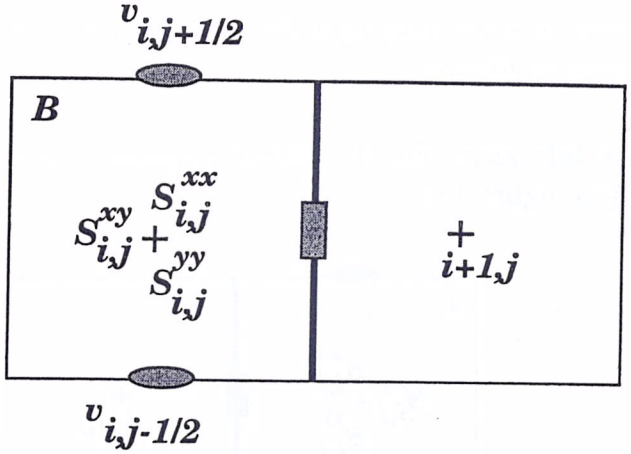

Fig. 11. Boundary cells having only the right side contiguous with an interior cell.

Considering figure 11, the values of the extra-stress components are obtained through equations (37)–(39) and are given by

$$S^{xx}_{i+\frac{1}{2},j} = 0 \tag{73}$$

$$S^{xy}_{i+\frac{1}{2},j}(t_{n+1}) = e^{-\frac{1}{We}\delta t} S^{xy}(t_n) + \left(1 - \frac{\lambda_2}{\lambda_1}\right) \frac{\partial v}{\partial y}(x_{i+\frac{1}{2}}, y_j, t^*) \left[e^{\frac{1}{We}\delta t} - 1\right] \tag{74}$$

$$S^{yy}_{i+\frac{1}{2},j}(t_{n+1}) = e^{-\frac{1}{We}\delta t} S^{yy}(t_n) + \delta t \frac{\partial v}{\partial y}(x_{i+\frac{1}{2}}, y_j, t^*) \left[e^{-\frac{1}{We}\delta t} S^{xy}(t_n) + S^{xy}(t_{n+1})\right] \tag{75}$$

where $\frac{\partial v}{\partial y}(x_{i+\frac{1}{2}}, y_j, t^*)$ is obtained by averaging $\frac{\partial v}{\partial y}(x_{i+\frac{1}{2}}, y_j, t)$ at times t_n and t_{n+1}, namely

$$\frac{\partial v}{\partial y}(x_{i+\frac{1}{2}}, y_j, t^*) = \frac{1}{2}\left[\frac{\partial v}{\partial y}(x_{i+\frac{1}{2}}, y_j, t_n) + \frac{\partial v}{\partial y}(x_{i+\frac{1}{2}}, y_j, t_{n+1})\right].$$

These derivatives are approximated by

$$\frac{\partial v}{\partial y}(x_{i+\frac{1}{2}}, y_j, t_n) = \frac{v^n_{i+1,j} - v^n_{i,j}}{\delta x}, \qquad \frac{\partial v}{\partial y}(x_{i+\frac{1}{2}}, y_j, t_{n+1}) = \frac{v^{n+1}_{i+1,j} - v^{n+1}_{i,j}}{\delta x}.$$

The velocities at cell positions (i, j) and $i+1, j)$ are given by

$$v_{i,j} = \frac{v_{i,j+\frac{1}{2}} + v_{i,j-\frac{1}{2}}}{2} \qquad \text{and} \qquad v_{i+1,j} = \frac{v_{i+1,j+\frac{1}{2}} + v_{i+1,j-\frac{1}{2}}}{2}, \text{ respectively.}$$

The required values of $S^{xx}_{i,j}$ and $S^{yy}_{i,j}$ are then computed by linear interpolation using the nodes $(i+\frac{1}{2}, j)$ and $(i+1, j)$.

Boundary cells having the left side contiguous with an interior cell are treated similarly.

5.4 Inflow and Outflow boundaries

On inflow boundaries it is assumed that $S^{xx} = S^{xy} = S^{yy} = 0$. In this case, the extra-stress components are given as follows:

Inflow (I) on the left side: For illustrative purposes it is assumed that the boundary is a vertical surface (see figure 12).

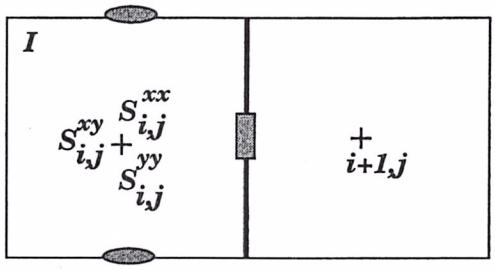

Fig. 12. Inflow cell with the right side contiguous with an interior cell.

In this case, the required values of the extra-stress components are given by (see Section 3.2)

$$S^{xx}_{i,j} = -S^{xx}_{i+1,j}, \qquad S^{xy}_{i,j} = -S^{xy}_{i+1,j}, \qquad S^{yy}_{i,j} = -S^{yy}_{i+1,j}$$

Other configurations of inflows (e.g. inflow on top side) are handled in a similar manner.

On outflow boundaries it is assumed that the homogeneous Neumann condition holds for S^{xx} and S^{yy} while S^{xy} is set to zero. In this case, the values of the non-Newtonian extra-stress components are obtained as follows.

Outflow (O) on the right side: Here we assume that the boundary is a vertical surface (see figure 13).

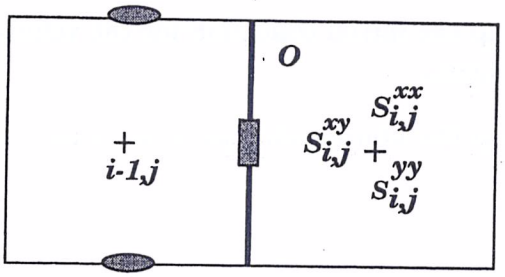

Fig. 13. Outflow cell with the right side contiguous with a interior cell.

Considering figure 13, the values of the extra-stress are given by

$$S^{xx}_{i,j} = S^{xx}_{i-1,j} \ , \qquad S^{xy}_{i,j} = S^{xy}_{i-1,j} \ , \qquad S^{yy}_{i,j} = S^{yy}_{i-1,j}$$

6. General comments

The finite difference equations described in this paper have been implemented into the GENSMAC code (see Tomé and McKee [12]) in order to simulate free surface flow of an Oldroyd-B fluid. The discretized momentum equations (56) and (57) are solved by the GENSMAC code; it was only necessary to modify the routine to include the terms involving the non-Newtonian component of the extra-stress tensor. The discretized Poisson equation (58), the final velocities (59) and the pressure equation (47) are solved as in the GENSMAC code as they do not change from those for a Newtonian fluid. A number of routines have been written to set up the boundary conditions on inflows, outflows, rigid boundaries and free surface. The following routines have been created:

- Tildevisco: this routine computes the tilde-velocities for an Oldroyd-B fluid according to equations (56) and (57).
- Extrastress: This routine calculates the components of the non-Newtonian extra-stress tensor **S** as given by equations (52)–(54).
- Ptildevisco: This routine sets the pressure on the surface cells according the finite difference equations derived in Section 5.2.

- InflowOutVisco: Sets the values of the non-Newtonian extra-stress components on inflows and outflow boundaries (see Section 5.4).
- Tanoutvisco: Computes the velocities on empty cells according the stress conditions given in Section 5.2.
- Surempvisco: Calculates the velocities on empty cell faces according to the equations derived in Section 5.2.
- Setboxvisco: Sets up the initial condition for the velocity field and the non-Newtonian extra-stress components.
- Bcondvisco: Sets up the non-Newtonian extra-stress on rigid boundaries (see Section 5.3)

7. Validation of the approach

7.1 Fully developed channel flow

We validate the treatment of the viscoelastic extra-stress tensor on rigid boundaries and on interior points by simulating the flow in a two-dimensional channel. We consider a 2D-channel formed by two parallel plates at a distance L from each other and having a length of $4L$ (see figure 14). At the channel entrance we impose fully developed flow and at the exit the conditions described in this paper for outflow boundaries are assumed. On the channel plates the no-slip condition and the expressions for the viscoelastic extra-stress tensor (see Section 3.1) are applied. We start with the channel empty and inject fluid at the inflow at a prescribed velocity. The fully developed flow imposed at the inflow is given by

$$u(y) = -6y(y - L), \qquad v = 0 \tag{76}$$

$$S^{xx}(y) = 2We\left(1 - \frac{\lambda_2}{\lambda_1}\right)\left(\frac{\partial u}{\partial y}\right)^2, \qquad S^{xy} = \left(1 - \frac{\lambda_2}{\lambda_1}\right)\left(\frac{\partial u}{\partial y}\right), \qquad S^{yy} = 0 \tag{77}$$

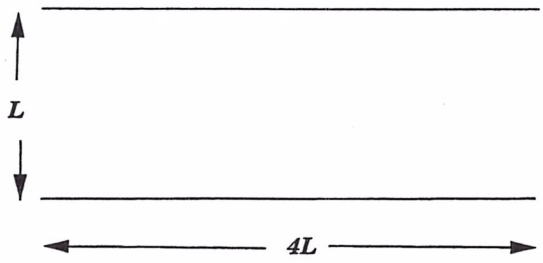

Fig. 14. Channel flow set up parameters.

Initialy the channel is empty and fluid is injected at the inflow until it reaches the outflow and steady state is established. Under steady state conditions the velocity field and the

viscoelastic extra-stress on the channel must have the same values as those on the inflow. To verify this, we performed one simulation for the Weissenberg number, $We = 1$. The input data used were $L = 1$, $U = 1$, $\delta x = \delta y = 0.25$, $\nu = 1$, $\lambda_1 = 1$ and the ratio λ_2/λ_1 was set equal to 0.5. In this run we have $Re = LU/\nu = 1$ and $We = \lambda_1 U/L = 1$. Figure 15 displays several snapshots taken from this simulation at different times. Figure 16 displays the values of the non-Newtonian extra-stress components S^{xx} and S^{xy} at the lines $x = 2$ (middle of the channel) and $x = 4$ (at the end of the channel) together with the respective analytic values (see eq. (77)). The solid lines in figure 16 are the analytical solutions while the dotted lines and the dotted-dashed lines are the numerical solutions of the extra-stress components at the positions $x = 2$ and $x = 4$ respectively. As can be see in figure 16 the agreement between the exact and the numerical solutions is very good. Indeed, the relative l_2-norm of the errors,

$$E^{xy} = \frac{\sum (S^{xy}_{exact} - S^{xy}_{numerical})^2}{\sum (S^{xy}_{exact})^2}, \qquad E^{xx} = \frac{\sum (S^{xx}_{exact} - S^{xx}_{numerical})^2}{\sum (S^{xx}_{exact})^2}$$

are $E^{xy} = 0.00038$ and $E^{xx} = 0.00179$ for $x = 2$ and $E^{xy} = 0.00022$ and $E^{xx} = 0.00093$ for $x = 4$.

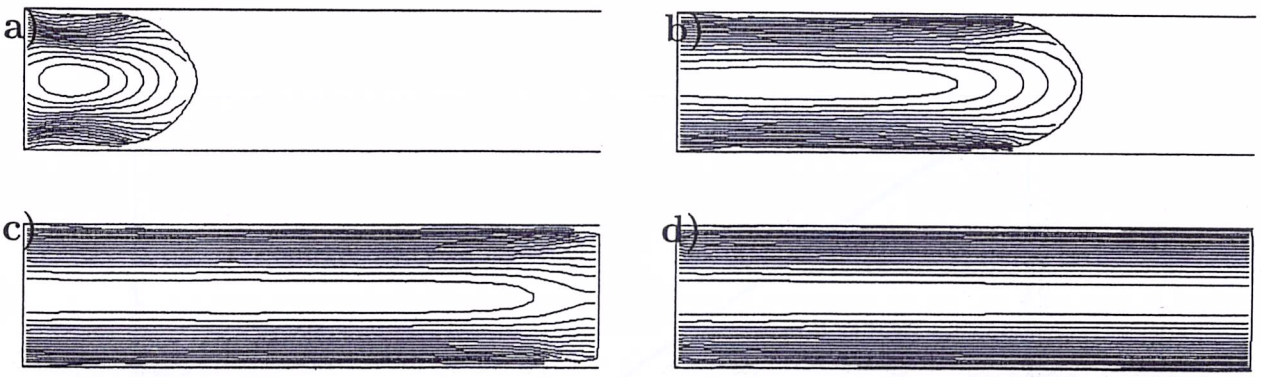

Figure 15. Numerical simulation of the channel flow. Fluid surface and velocity contours at times: **a)** t = 1.0, **b)** t = 2.5, **c)** t = 4.0 and **d)** t = 49.5.

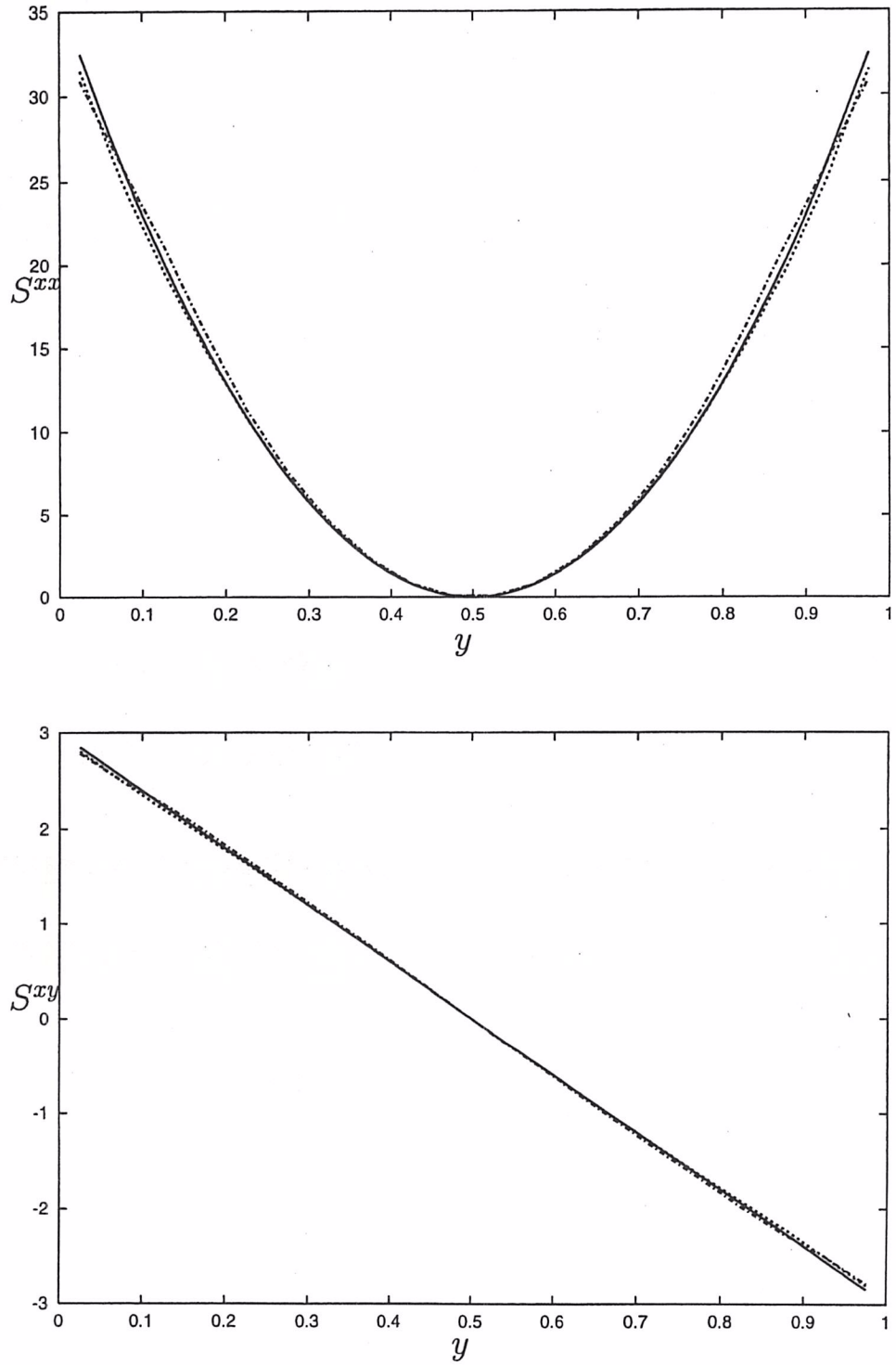

Figure 16. Numerical and analytical solutions of S^{xy} and S^{xx} at time $t = 49.5$ at positions $x = 2$ and at $x = 4$. The dotted-dashed line represents the numerical solution at $x = 2$ while the dotted line displays the numerical solution obtained at $x = 4$. The solid lines represent the exact solutions given by (77).

7.2 Start-up Couette flow

Mompean and Deville [3] validated their finite volume approach for time dependent start-up Couette flow of a Newtonian and an Oldroyd-B fluid. They compared their numerical solutions to the analytic solution for this problem as given by Schaftingen [30]. We shall employ this analytic solution to validate the procedure presented in Section 3 and the boundary stress treatment (see Section 3.1).

We simulated the shear flow sketched in figure 17. In this problem, the upper plate is moved from rest to velocity U instantaneously, producing the so-called start-up Couette flow. Following Mompean and Deville [3], figure 17 shows three equidistant points used to observe the time evolution of the velocity. For an Oldroyd-B fluid the exact solution for the velocity field is found to be (see Schaftingen [30])

$$\frac{u}{U} = \frac{y}{L} + \frac{2}{\pi}\sum_{n=1}^{\infty}\frac{(-1)^n}{n}\sin\left(n\pi\frac{y}{L}\right)T_n(t) \tag{78}$$

where

$$T_n(t) = \exp\left(-\frac{\gamma_n t}{2}\right)\left[\cos(\omega_n t) + \left(\frac{\gamma_n}{2\omega_n} - \frac{n^2\pi^2\mu_2}{\rho L^3\omega_n}\right)\sin(\omega_n t)\right] \quad \text{if} \quad \gamma_n^2 - \frac{4n^2\pi^2\mu_0}{\rho\lambda_1 L^2} < 0$$

or

$$T_n(t) = \frac{\left(\beta_{2n} + n^2\pi^2\frac{\mu_2}{\rho L^2}\right)\exp(\beta_{1n}t) - \left(\beta_{1n} + n^2\pi^2\frac{\mu_2}{\rho L^2}\right)\exp(\beta_{2n}t)}{\beta_{2n} - \beta_{1n}} \quad \text{if} \quad \gamma_n^2 - \frac{4n^2\pi^2\mu_0}{\rho\lambda_1 L^2} \geq 0$$

where

$$\gamma_n = \frac{1}{\lambda_1} + \frac{n^2\pi^2\mu_2}{\rho\lambda_1 L^2}, \quad \omega_n = \frac{\sqrt{\frac{4n^2\pi^2\mu_0}{\rho\lambda_1 L^2} - \gamma_n^2}}{2}, \quad \beta_{1n} = \frac{\sqrt{\gamma_n^2 - \frac{4n^2\pi^2\mu_0}{\rho\lambda_1 L^2}} - \gamma_n^2}{2}, \quad \beta_{2n} = -\gamma_n - \beta_{1n}. \tag{79}$$

The viscosities appearing in equations above are related to the Oldroyd-B model by setting $\mu_1 = \left(1 - \frac{\lambda_2}{\lambda_1}\right)\mu_0$, $\mu_2 = \left(\frac{\lambda_2}{\lambda_1}\right)\mu_0$, where μ_0 is called the solvent viscosity. By making $\lambda_2 = \lambda_1$ a Newtonian flow is obtained. We used the problem described above and carried out a Newtonian validation by setting $\lambda_2 = \lambda_1$ in the Oldroyd-B model and performed three simulations. We set $L = 1$ and $U = 1$. A grid of 10×20 cells ($\delta x = \delta y = 0.05$) was used for all these runs and a time-step of

$$\begin{cases} \delta t = 0.25 Re \delta y^2 \text{ if } Re < 1 \\ \delta t = 0.25 \delta y^2 \text{ otherwise} \end{cases}$$

was employed. Figure 18, displays the numerical velocity profiles obtained together with the analytical solution given by (78) for Re $= 0.5$, 1.0 and Re $= 5$ (we used $\mu_0 = 2,1$ and $\mu_0 = 0.2$, respectively). The numerical results are in excellent agreement with the analytical solution: indeed, from figure 18 we see that the numerical and analytic solutions coincide. We can see in Figure 18 that the time for the velocity profile becoming linear is $t = 0.2$ for Re $= 0.5$, $t = 0.4$ for Re $= 1$ and $t = 2$ for Re $= 5$ displaying a linear dependence on the Reynolds number.

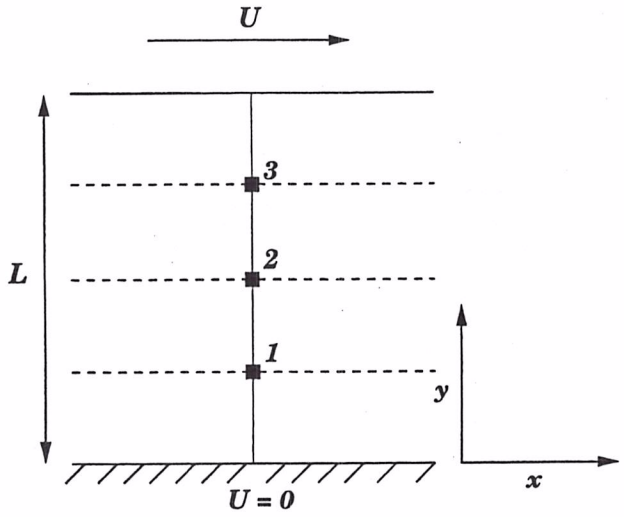

Figure 17. Flow geometry for the start up Couette flow.

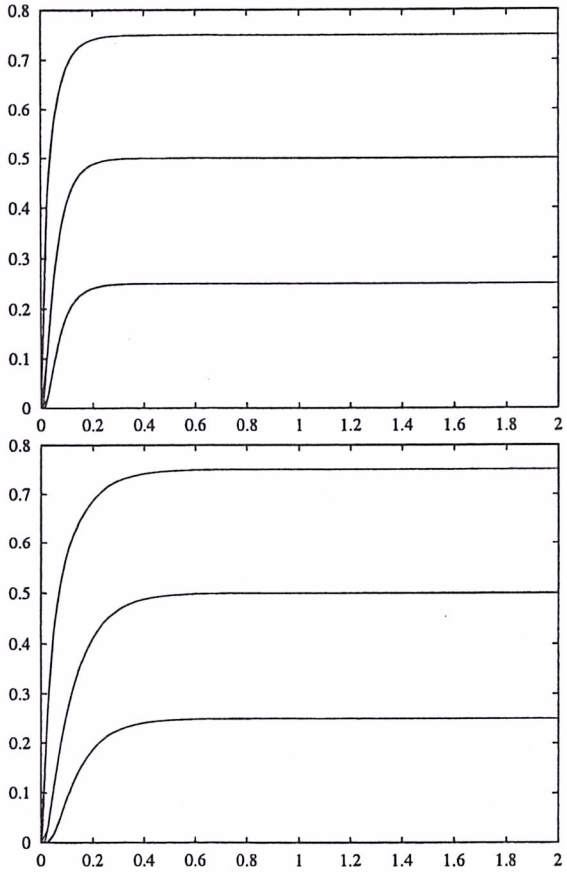

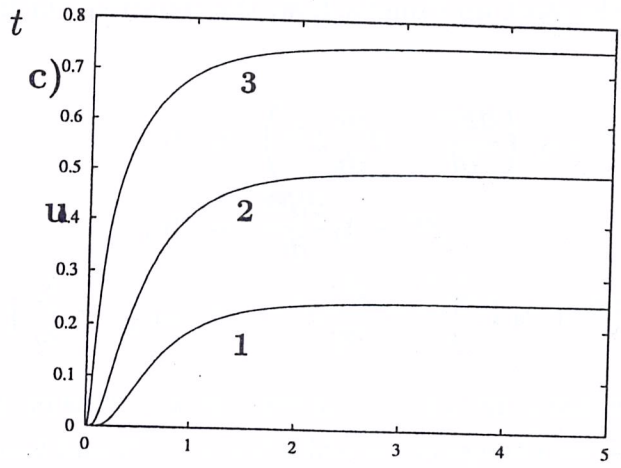

Figure 18. Velocity variation at spatial positions 1, 2 and 3 (see figure 17) for a Newtonian fluid in a start-up shear flow for various Reynolds numbers: **a)** Re = 0.5 , **b)** Re = 1.0 **c)** Re = 5.0

7.3 Oldroyd-B validation

One can see that for the start up Couette flow, the equations for the extra-stress components (7)–(9) reduce to

$$S^{xx} + \lambda_1 \left(\frac{\partial S^{xx}}{\partial t} - 2\frac{\partial u}{\partial y} S^{xy} \right) = 0 , \tag{80}$$

$$S^{yy} + \lambda_1 \frac{\partial S^{yy}}{\partial t} = 0 , \tag{81}$$

$$S^{xy} + \lambda_1 \left(\frac{\partial S^{xy}}{\partial t} - \frac{\partial u}{\partial y} S^{yy} \right) = \mu_0 \left(1 - \frac{\lambda_2}{\lambda_1} \right) \left(\frac{\partial u}{\partial y} \right) . \tag{82}$$

By using the solution given by (78) we can find the solutions of (80)–(82). We proceed as in Section 3.1 and make the change of variables $\mathbf{S} = e^{-\frac{1}{\lambda_1}t}\tilde{\mathbf{S}}$ and transform equations (80)–(82) into

$$\frac{\partial \tilde{S}^{xx}}{\partial t} - 2\frac{\partial u}{\partial y}\tilde{S}^{xy} = 0 , \tag{83}$$

$$\frac{\partial \tilde{S}^{yy}}{\partial t} = 0 , \tag{84}$$

$$\frac{\partial \tilde{S}^{xy}}{\partial t} - \frac{\partial u}{\partial y}\tilde{S}^{yy} = \frac{\mu_0}{\lambda_1} \left(1 - \frac{\lambda_2}{\lambda_1} \right) e^{\frac{1}{\lambda_1}t} \frac{\partial u}{\partial y} , \tag{85}$$

respectively. Equations (83)–(85) together with the initial condition $\mathbf{S} = \mathbf{0}$ can be solved. Firstly, from (84) we obtain

$$\tilde{S}^{yy} = 0$$

and (85) can then be written as

$$\tilde{S}^{xy} = \int_0^t \frac{\mu_0}{\lambda_1} \left(1 - \frac{\lambda_2}{\lambda_1} \right) e^{\frac{1}{\lambda_1}s} \frac{\partial u}{\partial y} ds . \tag{86}$$

Introducing (78) into (86) we get

$$\begin{aligned} \tilde{S}^{xy} &= \frac{V\mu_0}{\lambda_1 L} \left(1 - \frac{\lambda_2}{\lambda_1} \right) \int_0^t e^{\frac{1}{\lambda_1}s} \left[1 + 2\sum_{n=1}^{\infty} (-1)^n \cos\left(\frac{n\pi y}{L} \right) T_n(s) \right] ds \\ &= \frac{V\mu_0}{\lambda_1 L} \left(1 - \frac{\lambda_2}{\lambda_1} \right) \left[\lambda_1 e^{\frac{1}{\lambda_1}t} - \lambda_1 + 2\sum_{n=1}^{\infty} (-1)^n \cos\left(\frac{n\pi y}{L} \right) \int_0^t e^{\frac{1}{\lambda_1}s} T_n(s) ds \right] \end{aligned}$$

which after integration we obtain

$$\tilde{S}^{xy} = \frac{V\mu_0}{L} \left(1 - \frac{\lambda_2}{\lambda_1} \right) \left(e^{\frac{1}{\lambda_1}t} - 1 \right) + 2\frac{V\mu_0}{\lambda_1 L} \left(1 - \frac{\lambda_2}{\lambda_1} \right) \sum_{n=1}^{\infty} (-1)^n \cos\left(\frac{n\pi y}{L} \right) I_n(t) \tag{87}$$

where $I_n(t) = \int_0^t e^{\frac{1}{\lambda_1}s} T_n(s)ds$ and is given by

$$I_n(t) = \frac{e^{-\alpha_n t}}{\alpha_n^2 + \beta_n^2}\left[\beta_n \sin(\beta_n t) - \alpha_n \cos(\beta_n t) - R_n\left(\alpha_n \sin(\beta_n t) + \beta_n \cos(\beta_n t)\right)\right] ,$$

$$\text{if } \gamma_n^2 - \frac{4n^2\pi^2\mu_0}{\rho\lambda_1 L^2} < 0$$

or

$$I_n(t) = \frac{\left(\beta_{2n} + \frac{n^2\pi^2\mu_2}{\rho L^2}\right)\frac{\lambda_1}{1+\lambda_1\beta_{1n}} e^{\frac{1+\lambda_1\beta_{1n}}{\lambda_1}t} - \left(\beta_{1n} + \frac{n^2\pi^2\mu_2}{\rho L^2}\right)\frac{\lambda_1}{1+\lambda_1\beta_{2n}} e^{\frac{1+\lambda_1\beta_{2n}}{\lambda_1}t}}{\beta_{2n} - \beta_{1n}}, \text{ if } \gamma_n^2 - \frac{4n^2\pi^2\mu_0}{\rho\lambda_1 L^2} \geq 0$$

where

$$\alpha_n = \frac{\gamma_n}{2} - \frac{1}{\lambda_1}, \qquad \beta_n = \omega_n, \qquad R_n = \frac{\gamma_n}{2\omega_n} - \frac{n^2\pi^2\mu_2}{\rho L^3 \omega_n} .$$

Having computed $\widetilde{S}^{xy}$ using (87) the value of S^{xy} is given by

$$S^{xy}(y,t) = e^{-\frac{1}{\lambda_1}t}\widetilde{S}^{xy} . \tag{88}$$

We considered the Couette flow described in Section 7.2 and used the analytic solutions given by (78) and (88) to validate the numerical method presented in this paper. This validation was carried out by varying the Reynolds number and the Weissenberg number ($We = \lambda_1 U/L$). The input data were the same as those employed for the Newtonian validation; only the data regarding the non-Newtonian extra stress tensor was changed. We used $\lambda_1 = 1, 10, 100$ producing Weissenberg numbers of $We = 1, 10, 100$, respectively. The ratio λ_2/λ_1 was kept constant and equal to 0.1. A time-step size of

$$\begin{cases} \delta t = 0.25\dfrac{Re}{We}\delta y^2 \text{ if } Re < 1 \\ \\ \delta t = 0.25\dfrac{1}{We}\delta y^2 \text{ otherwise} \end{cases}$$

was employed. We varied the the Weissenberg number and the Reynolds number. In total 9 runs were performed for $We = 1, 10, 100$ and $Re = 0.5, 1, 5$. For each run we printed the time evolution of the velocity and the non-newtonian extra-stress component S^{xy} at the 3 points shown in figure 17. The results are displayed in figure 19, figure 20 and figure 21. Figure 19 displays the results for $Re = 0.5$ and figure 20 shows the results for $Re = 1$ while the results for $Re = 5$ are displayed in figure 21. As we can see, the agreement between the numerical solutions and the analytic solutions are excellent: the numerical solution is overlaid on top of the analytic solution and so, to the accuracy of the printer, the numerical results appear exact.

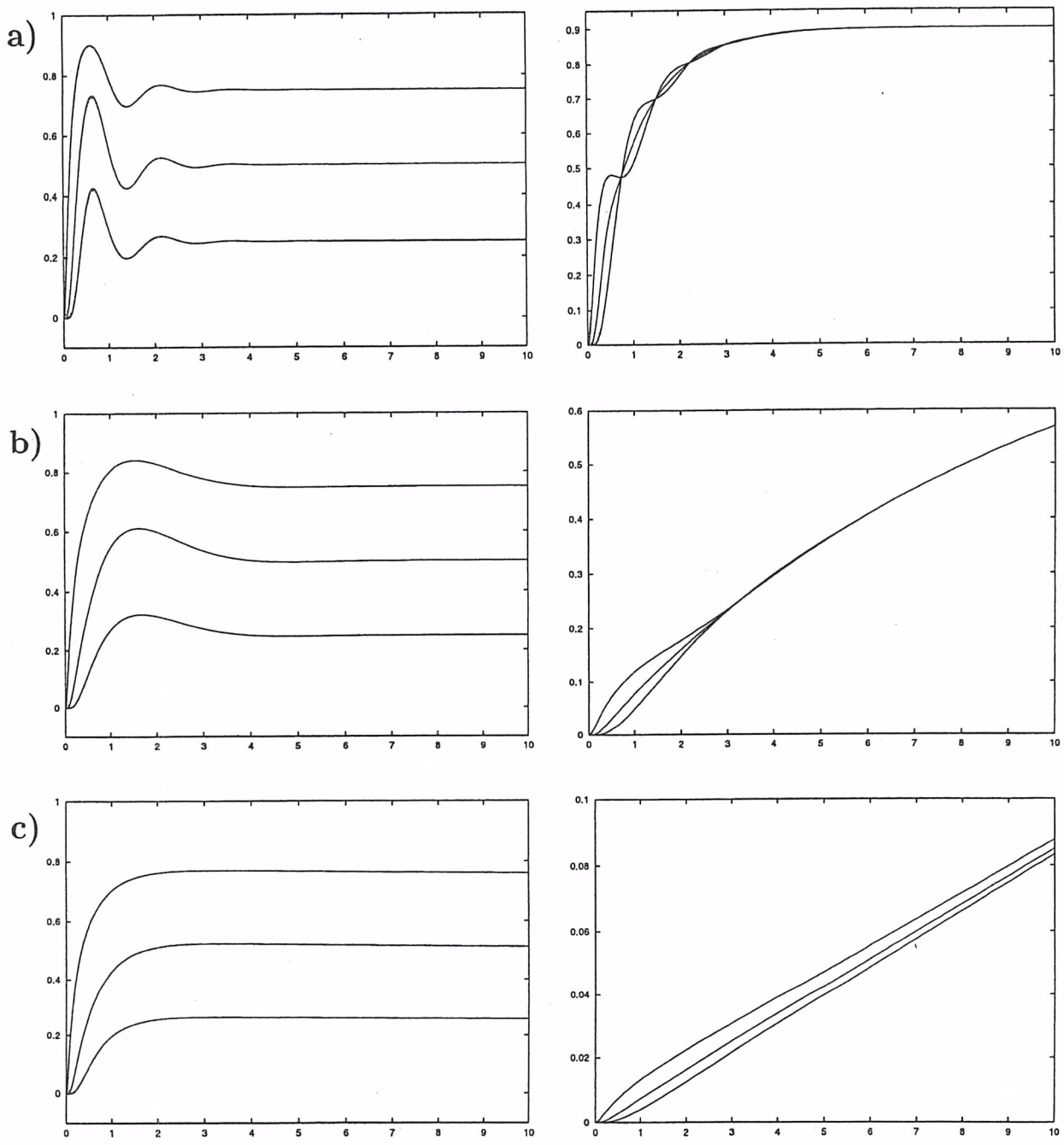

Figure 19. Time evolution of the start up Couette flow. Comparison between the analytical and the numerical solutions. Velocity variation (left column) and the non-Newtonian extra-stress component S^{xy} (right column). Reynolds number $Re = 0.5$ and various Weissenberg numbers:
a) $We = 1$, b) $We = 10$, c) $We = 100$.

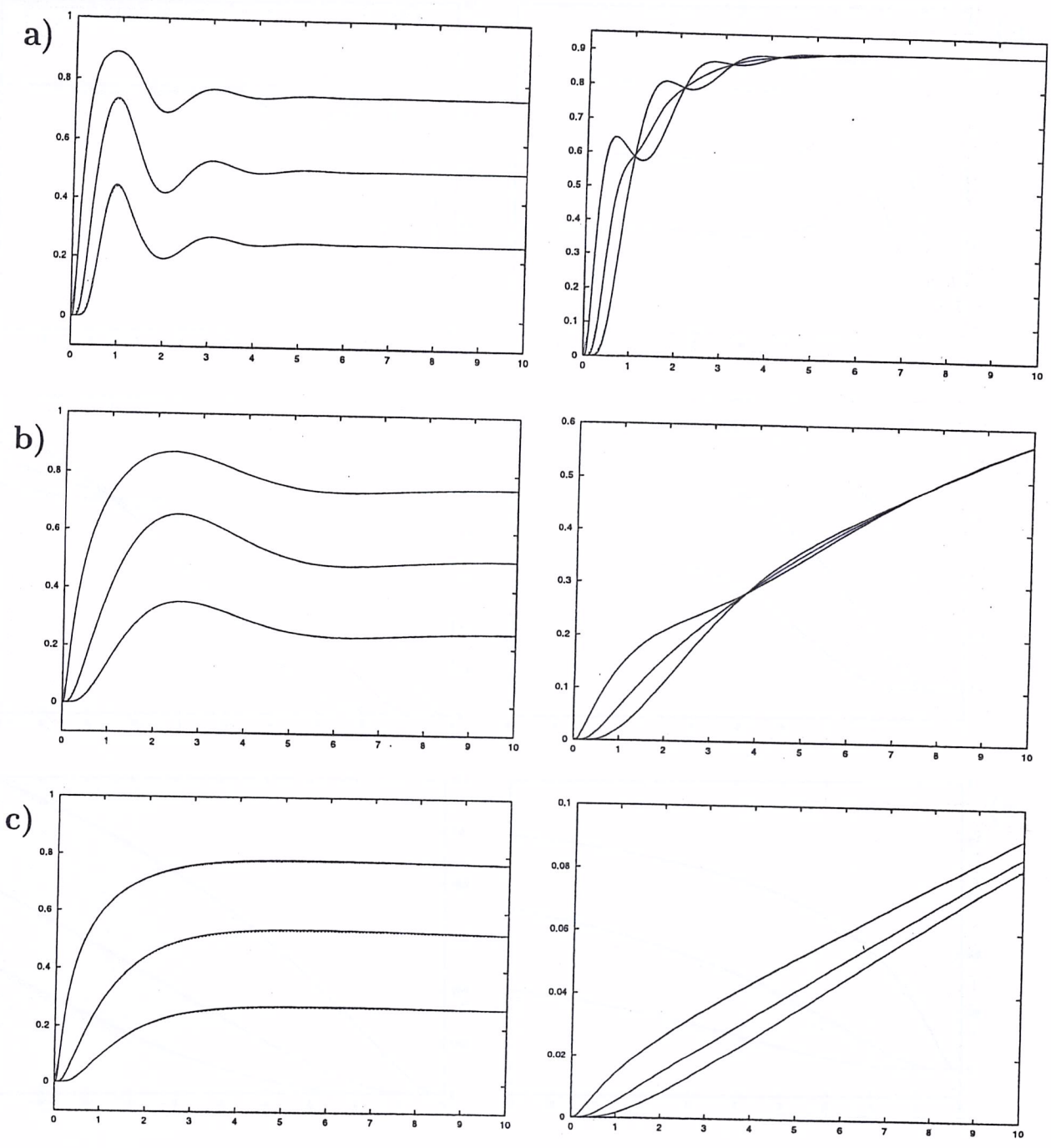

Figure 20. Time evolution of the start up Couette flow. Comparison between the analytical and the numerical solutions. Velocity variation (left column) and the non-Newtonian extra-stress component S^{xy} (right column). Reynolds number $Re = 1$ and various Weissenberg numbers:
a) $We = 1$, b) $We = 10$, c) $We = 100$.

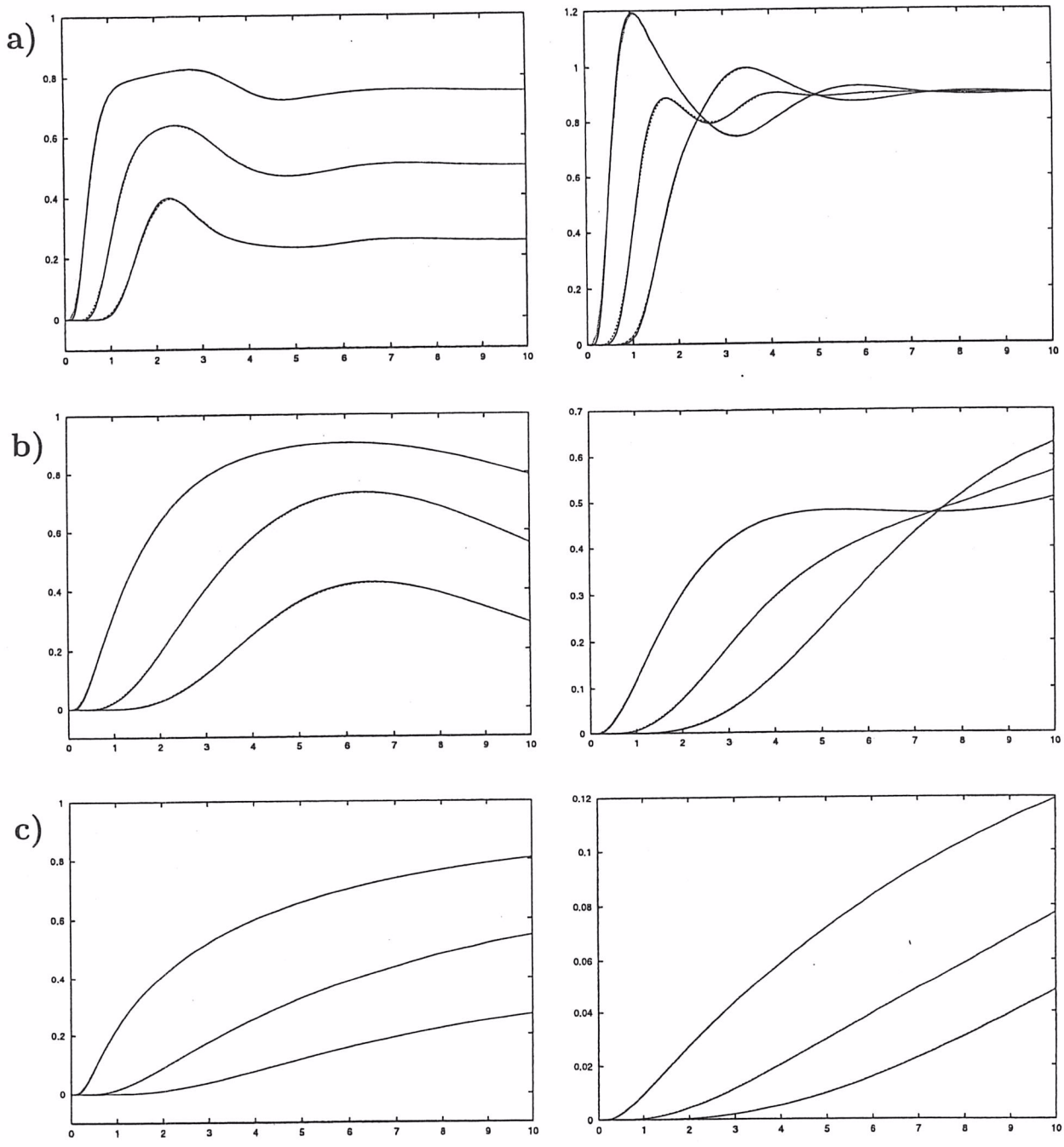

Figure 21. Time evolution of the start up Couette flow. Comparison between the analytical and the numerical solutions. Velocity variation (left column) and the non-Newtonina extra-stress component S^{xy} (right column). Reynolds number $Re = 5$ and various Weissenberg numbers:
a) $We = 1$, b) $We = 10$, c) $We = 100$.

8. Numerical examples of unsteady viscoelastic free surface flows

To demonstrate that the technique presented in this paper can cope with unsteady viscoelastic free surface flows we present three problems which clearly display viscoelastic behaviour. In each case the ratio λ_2/λ_1 was set to unity to represent a Newtonian fluid.

8.1 Numerical simulation of the transient extrudate swell of a planar jet

We present a simulation of the flow of a planar jet emerging from a die which exhibits the characterist phenomenon known as "extrudate swell' or "jet swell". This problem has attracted the attention of many researchers and various techniques for the simulation of jet swell have been proposed (e.g. [4], [34], [35], [36]).

We consider the time-dependent flow of a two-dimensional jet flowing through a slit and extrudated into air. The no-slip condition is imposed on the wall of the slit while full developed flow is imposed at the fluid entrance (see equations (76) and (77)). On the fluid free surface we imposed the full stress conditions (see (61) and (62)). The flow domain is sketched in figure 22.

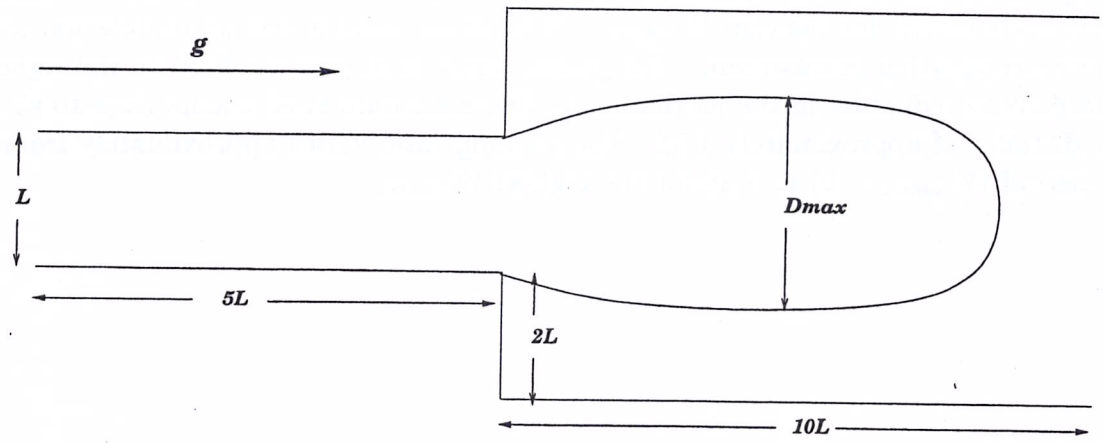

Fig. 22. Definition of the flow domain for the extrudate swell simulation.

The following input data were employed:

- Slit width: $L = 10$ mm.
- $\delta x = \delta y = 0.5$ mm
- Poisson solver tolerance $EPS = 10^{-10}$.
- Gravity is acting in the x-direction with $g = 9.81\text{m}^2\text{s}^{-1}$.
- Fluid definition: $\mu_0 = 0.01$, $\rho = 1$, $\lambda_1 = 0.01$, $\lambda_2 = 0.0075$, 0.005 and 0.0025.

- Scaling parameters: $L = 0.01$, $U = 1$, $\mu_0 = 0.01$. Hence, $Re = 1$ and $We = 1$.

To demonstrate that the technique presented in this paper can cope with viscoelastic fluids governed by the Oldroyd-B model, we used the data above and performed three simulations. The first simulation we set $\lambda_2 = 0.75\lambda_1$; in the second simulation a value of $\lambda_2 = 0.5\lambda_1$ was employed and in the third simulation we chose $\lambda_2 = 0.25\lambda_1$. At this point we observe that the value of $We = 1$ used in these simulations is not the effective Weissenberg number. The effective Weissenberg number for the Oldroyd-B model, as pointed out by Yoo and Na [1], is

$$We_{\text{effect}} = \left(1 - \frac{\lambda_2}{\lambda_1}\right) We \, .$$

Thus, in these simulations we used $We_{\text{effect}} = 0.25, 0.5, 0.75$, respectively. The results of these simulations are displayed in figure 23 and figure 24. Figure 23 shows different time frames of the jet flowing through the slit and then being extrudated into the air. The swelling ratio $S_r = D_{max}/L$ is also shown in the figures. For the times $t = 2$ and $t = 4.5$ the flow is still inside the slit and the differences between the three cases are small. However, as the jet is extrudated into the air the differences are noticeable as we can see by comparing the size of the jet swelling for the three cases. Figure 24 shows the jet at the later time $t = 24.5$ after entering the outflow boundary. At this time the flow is close to reaching the steady state except for the case $We_{\text{effect}} = 0.25$ where there is still an undulation on the free surface propagating downstream. The gravity effect is to pull the fluid to the right causing a downstrean reduction in the jet diameter. The maximum swell occurs close to the slit exit at a distance of approximately $1.5L$. The swelling ratio varies approximately from 1.06 (in the case of $We_{\text{effect}} = 0$) to 1.88 for the highest We_{effect}.

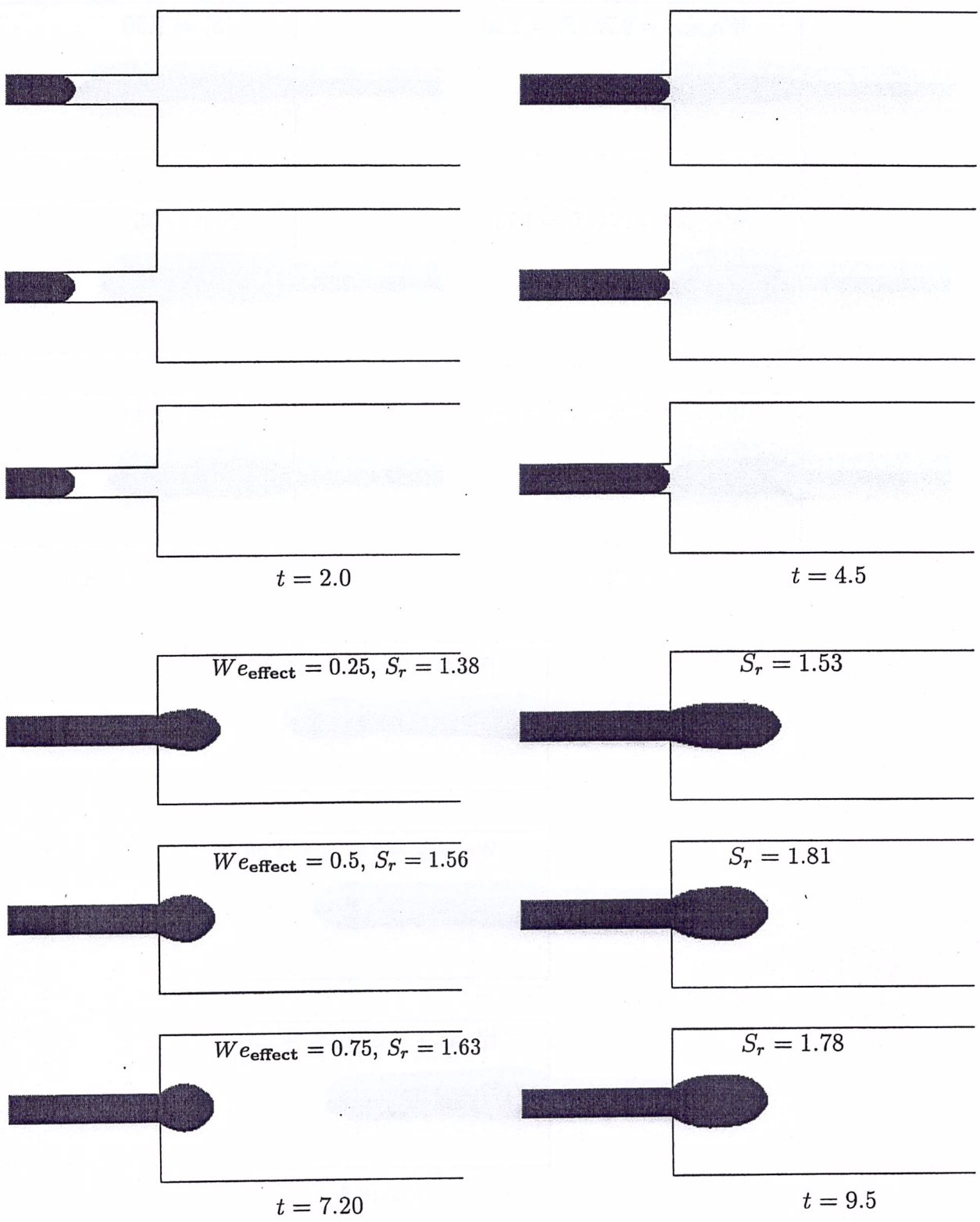

Figure 23. Numerical Simulation of the extrudate swell. Fluid surface and swelling ratio ($S_r = D_{max}/L$) at different times for $We_{\text{effect}} = 0.25, 0.5$, and 0.75. At times $t = 2.0$ and $t = 4.5$ the swelling ratio is $S_r = 1$ (as the jet has not yet been extrudated into the air).

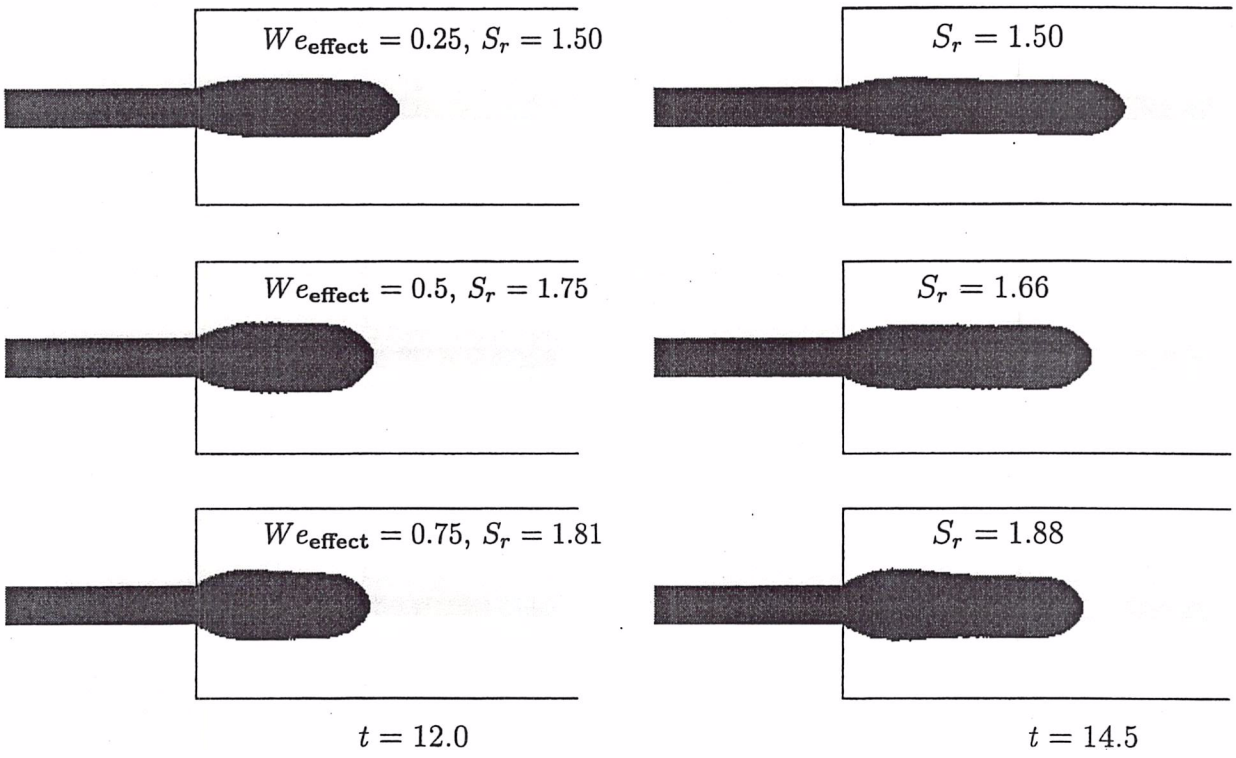

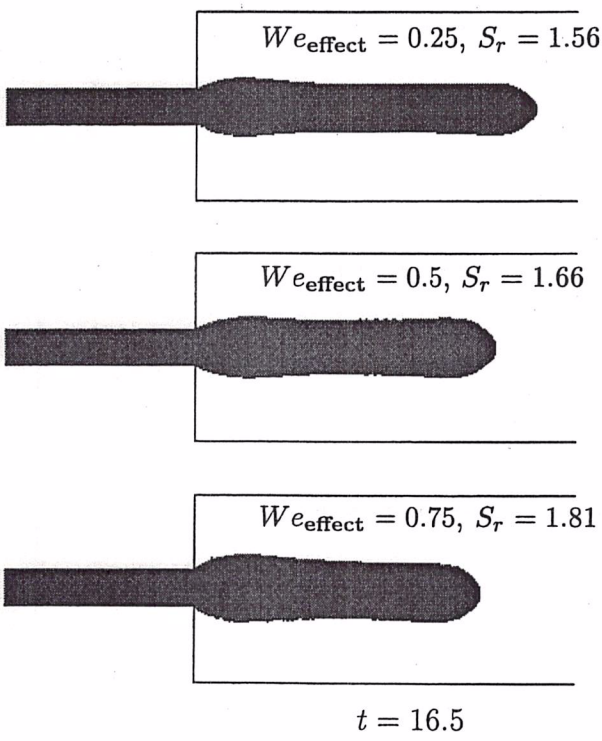

Figure 23. Continued.

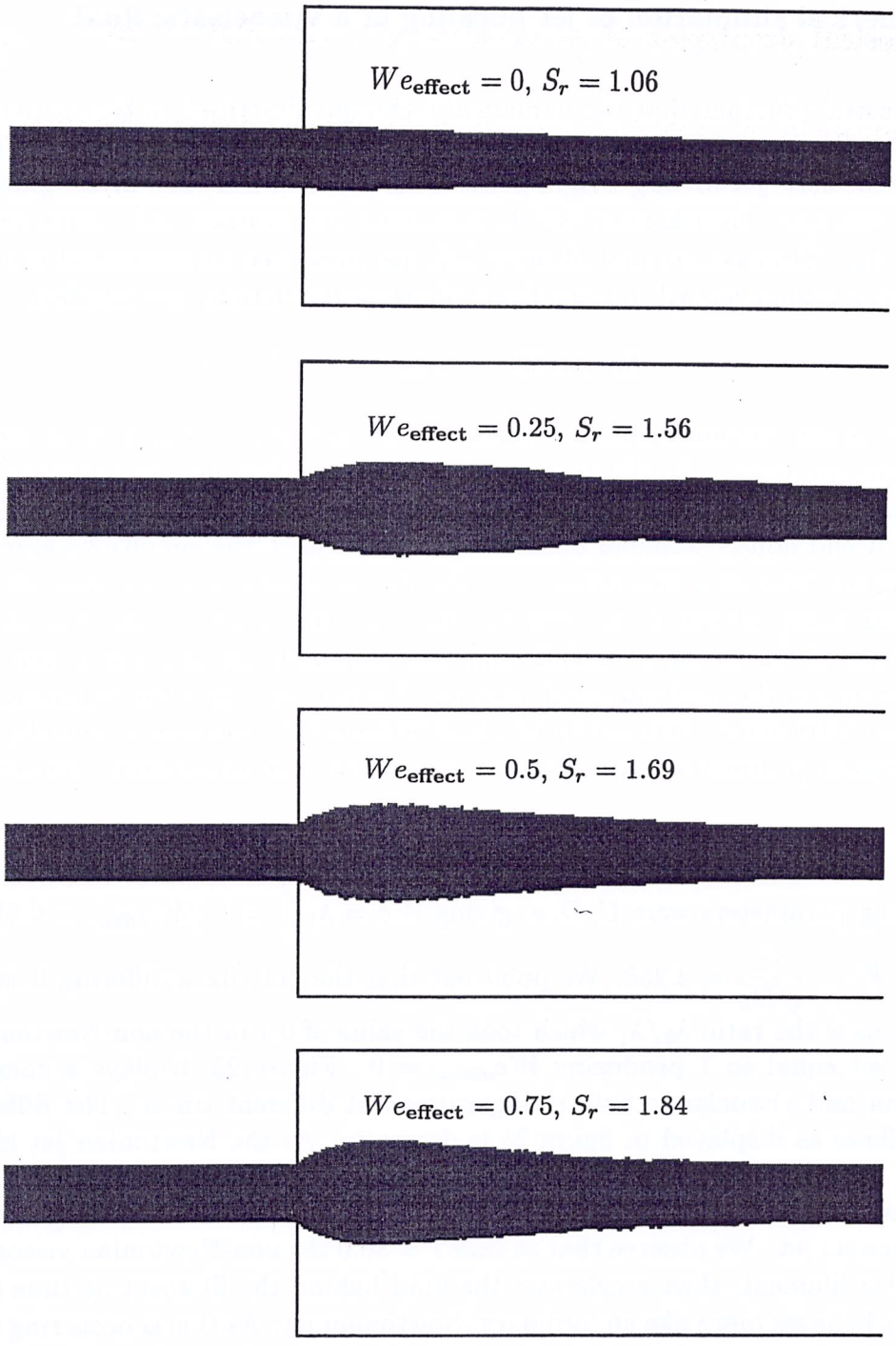

Figure 24. Numerical Simulation of the extrudate swell. Fluid surface and swelling ratio at time $t = 24.5$ for $We_{\text{effect}} = 0.0, 0.25, 0.5,$ and 0.75.

8.2 Numerical simulation of jet buckling of a viscoelastic fluid.

To demonstrate further that the numerical technique described in this paper can cope with viscoelastic fluids, we present in this section two calculations that simulate the buckling of a thin viscoelastic jet hitting a rigid plate. This problem has been investigated by a number of researchers (e.g. Cruickshank [31], Cruickshank and Munson [32], Tomé and McKee [33]). In particular, Cruickshank and Munson [32] has presented experimental results where they argue that a planar jet will buckle if the following restrictions are satisfied:

$$Re < 0.56 \qquad \text{and} \qquad H/D > 3\pi \ ,$$

where Re is the Reynolds number based on the slit width D and H is the height of the inlet above the plate. To illustrate that a fluid modelled by the Oldroyd-B model has a considerable effect on the buckling phenomenon, we present two calculations that contrast Newtonian and non-Newtonian behaviour; in both cases, the conditions above are satisfied, predicting buckling of a Newtonian jet. The calculations concern a thin jet injected into a rectangular cavity of size 5 cm, with the inlet slot size of $D = 5$ mm (so that $H/D = 20$). A mesh size of $\delta x = \delta y = 0.0005$ mm was employed (giving 100×200 cells). At the inlet we imposed the uniform input velocity $U = 0.5$ ms^{-1} and the components of the non-Newtonian extra stress were set to zero (see Section 3.2). Gravity is considered to be acting in the negative y-direction with $g = 9.81$ ms^{-2}. The fluid parameters were chosen to be

$$\nu = 0.01 \ , \qquad \lambda_1 = 0.01 \ , \qquad \lambda_2 = 0.001 \ .$$

The scaling parameters were U, D, ν, giving $We = \lambda_1 \dfrac{U}{D} = 1$ ($We_{\text{effect}} = 0.9$), $Re = \dfrac{UD}{\nu} = 0.25$ and $Fr = \dfrac{U}{\sqrt{Dg}} = 2.258$. We point out that the only data differing between these two calculations is the ratio λ_2/λ_1 which took the value of 0.1 in the non-Newtonian calculation and was set equal to 1 producing $We_{\text{effect}} = 0$. Figure 25 displays a comparison of the Newtonian and viscoelastic fluid configurations at different times. The difference between the two flows as displayed in figure 25 is dramatic. As the Newtonian jet hits the plate it becomes thicker while the non-Newtonian jet produces a wave which travels upwards along the jet creating an instability which causes the jet to buckle dramatically much earlier than the Newtonian jet. We observe that at time $t = 30.0$ the non-Newtonian viscoelastic jet thins to almost a filament, then accelerates the fluid behind the filament at time $t = 36.25$, and thereafter behaves more like an 'ordinary' Newtonian jet. As this is occurring the Newtonian fluid jet continues to thicken at the base with only a hint of initial buckling at time $t = 30.0$. At the time the Newtonian jet starts to buckle the non-Newtonian jet has already produced many folds.

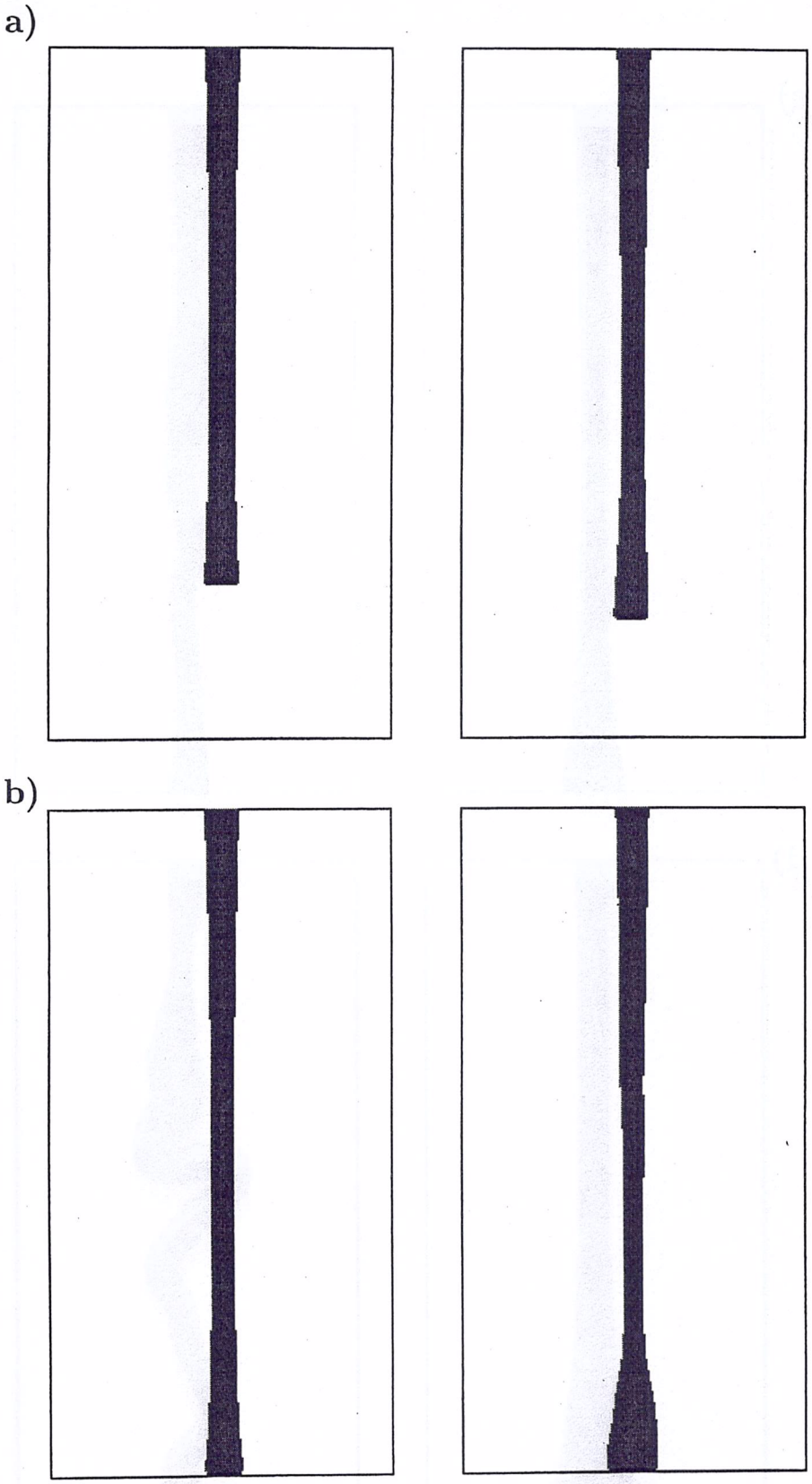

Figure 25. Numerical simulation of jet buckling. Fluid flow visualization at different times: Newtonian jet (on the left) and non-Newtonian (on the right). Times shown are ($\frac{U}{D}t$): **a)** 12.5, **b)** 15.0, **c)** 17.5, **d)** 23.75, **e)** 27.5, **f)** 30.0, **g)** 36.25, **h)** 42.5, **i)** 48.75, **j)** 55.0.

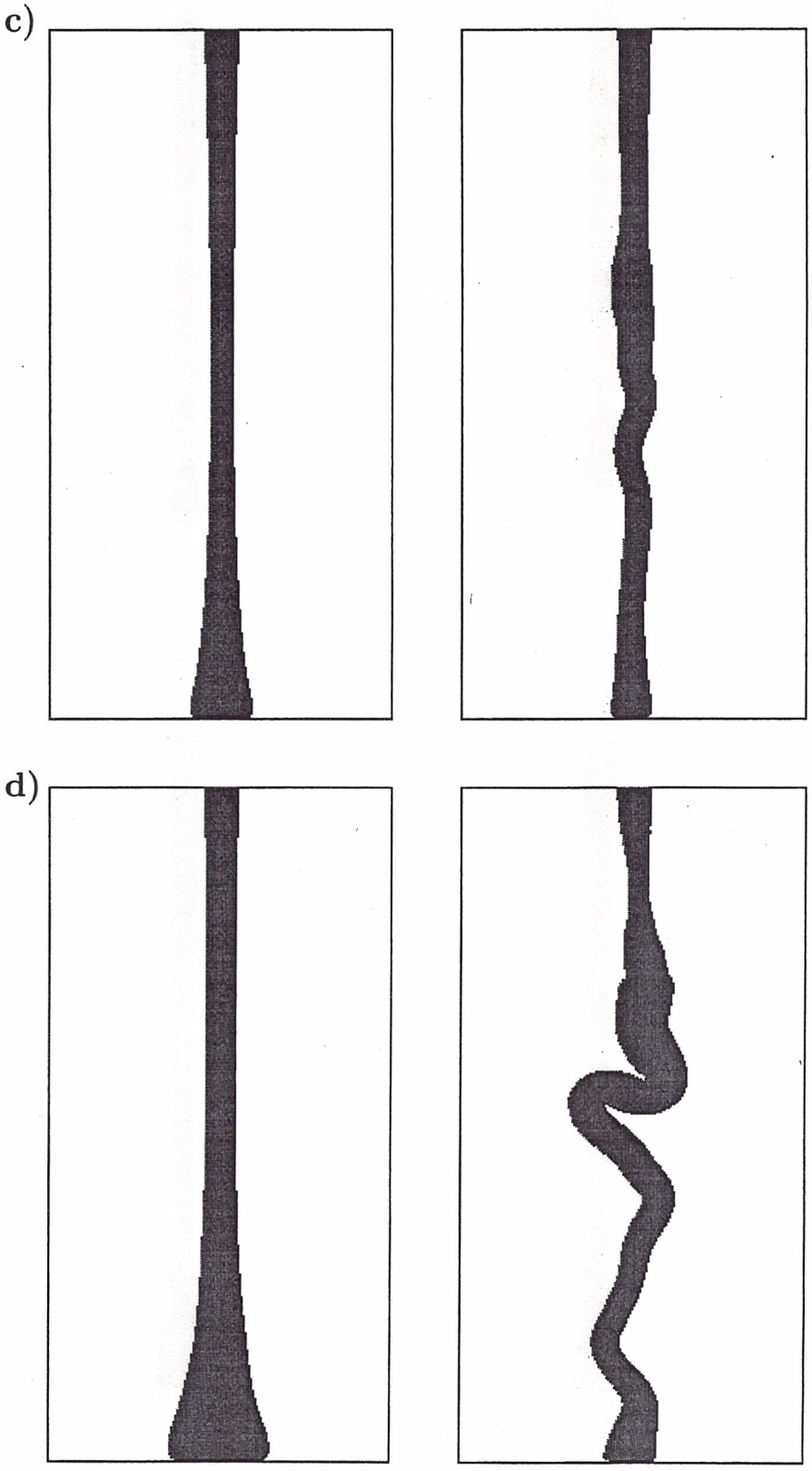

Figure 25. Continued.

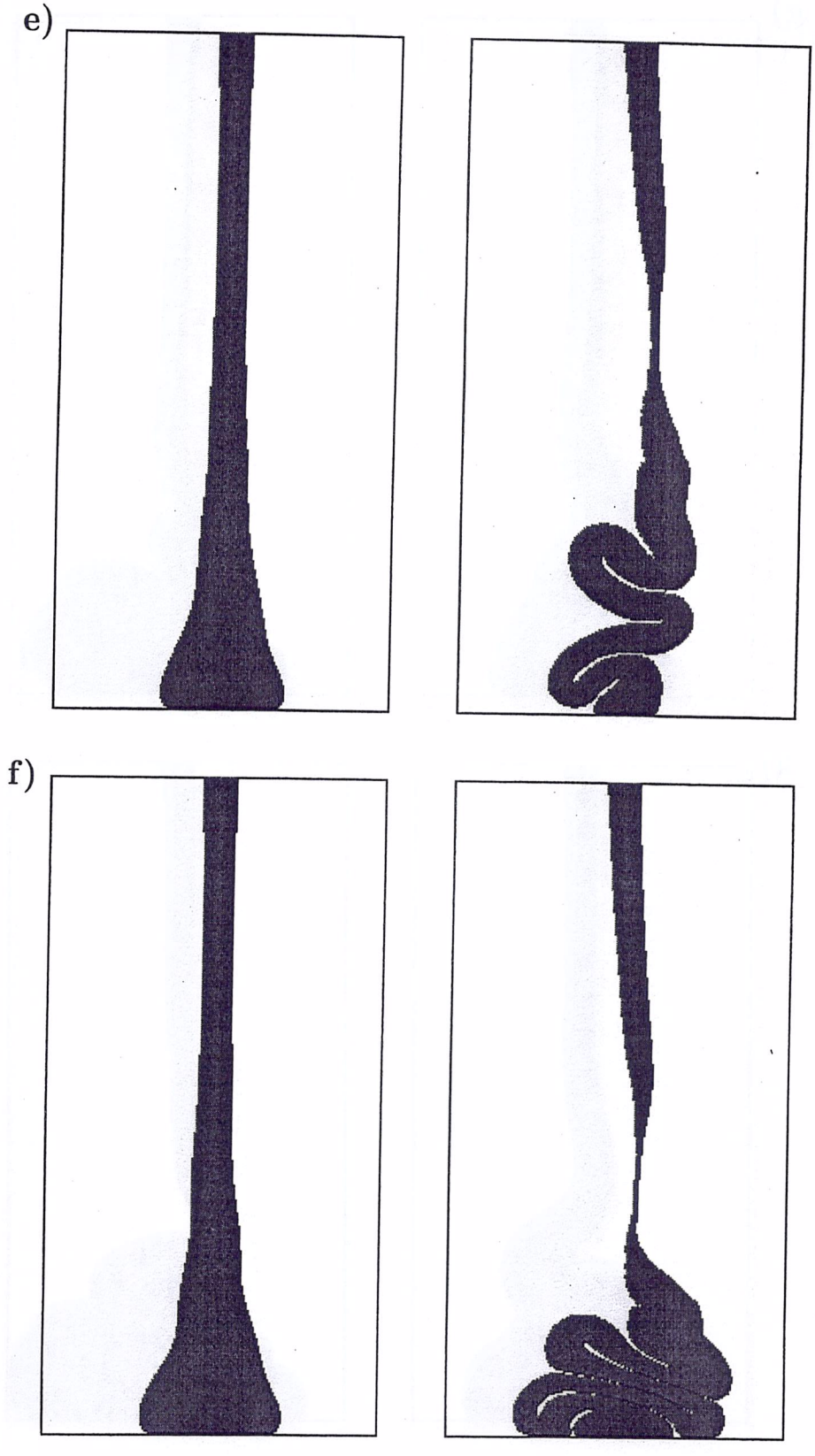

Figure 25. Continued.

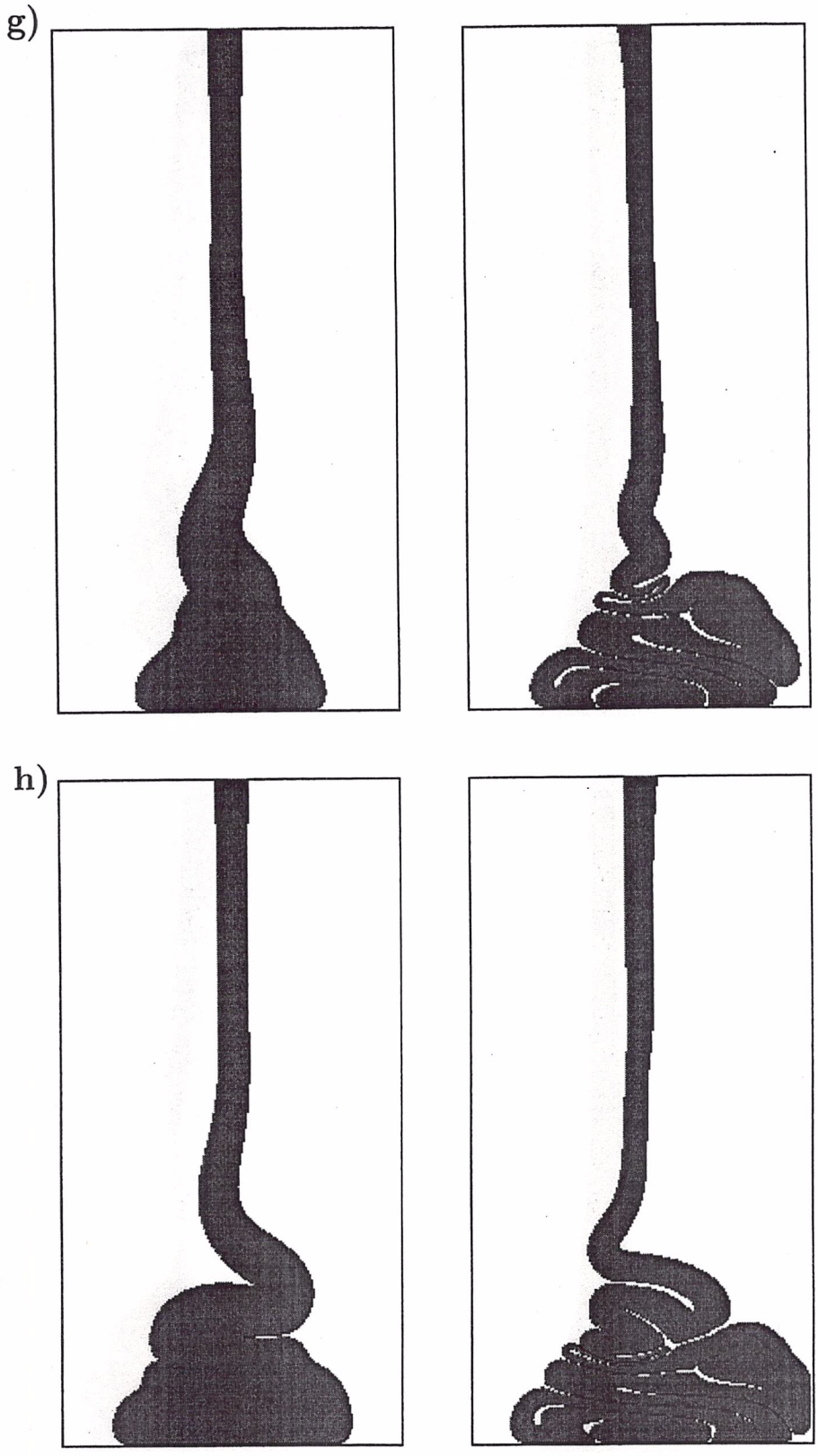

Figure 25. Continued.

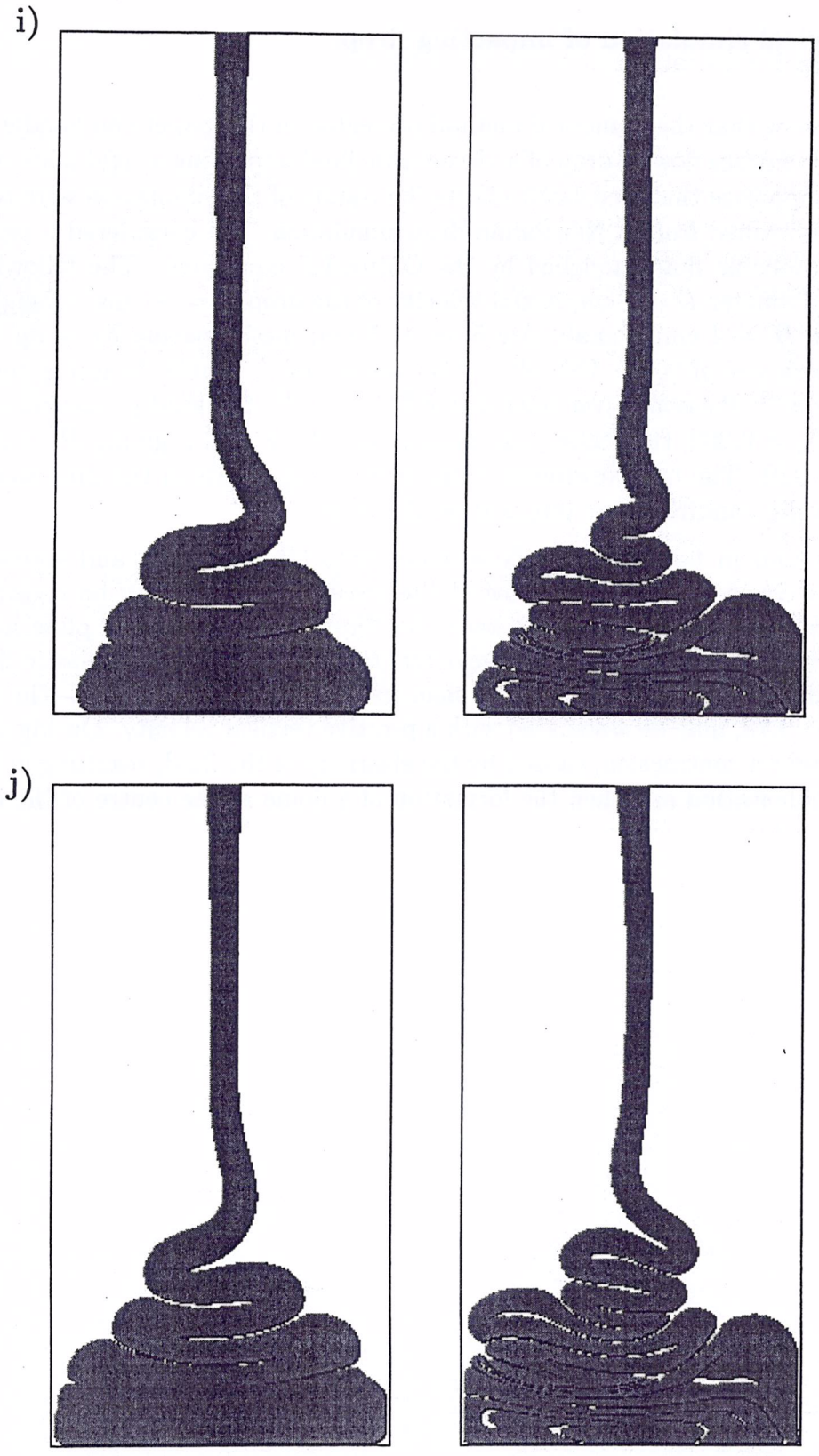

Figure 25. Continued.

8.3 Numerical simulation of impacting drop.

To further show that the numerical method presented in this paper can handle unsteady viscoelastic free surface flows a drop of a viscoelastic fluid impacting a rigid plate was simulated. Again, to emphasize the viscoelastic effects the results of the simulation were compared with the results obtained from a Newtonian drop simulation. We considered a two-dimensional drop of viscoelastic fluid modelled by the Oldroyd-B equations. The following data were used: drop diameter $D = 2$ cm; initial velocity of the drop $V = -1$ ms^{-1}; height of the drop to the plate $H = 4$ cm; domain size 5 cm $\times$ 5 cm; mesh spacing $\delta x = \delta y = 0.0005$ mm (giving a mesh size of 100 $\times$ 100 cells within the domain); gravity is acting downwards with $g = -9.81$ ms^{-2}; Poisson solver tolerance $EPS = 10^{-10}$; the fluid properties are $\nu = 0.004$, $\lambda_1 = 0.02$, $\lambda_2 = 0.002$; the scaling parameters were D, V and ν giving $Re = 5$ and $We = 1$ ($We_{\text{effect}} = 0.9$). The non-Newtonian extra stress components in the drop were initially set to zero. No-slip conditions are imposed on the plate.

As may be seen in figure 26, the Newtonian drop hits the plate and spreads out evenly retaining its concave shape. The flow of the viscoelastic drop may be regarded as having three phases. The initial phase, between the time the drop hits the plate and $t = 2.5$, is associated with the negative vertical velocity. In this phase the viscoelastic flow displays a greater tendency to spread horizontally than its Newtonian counterpart. The second phase, for $2.5 < t < 3.75$, may be associated with a positive vertical velocity. During this phase, the flow underwent a contraction, caused by the elasticity of the fluid, resulting in the formation first of an indentation and then the formation of a dome at the centre of the domain.

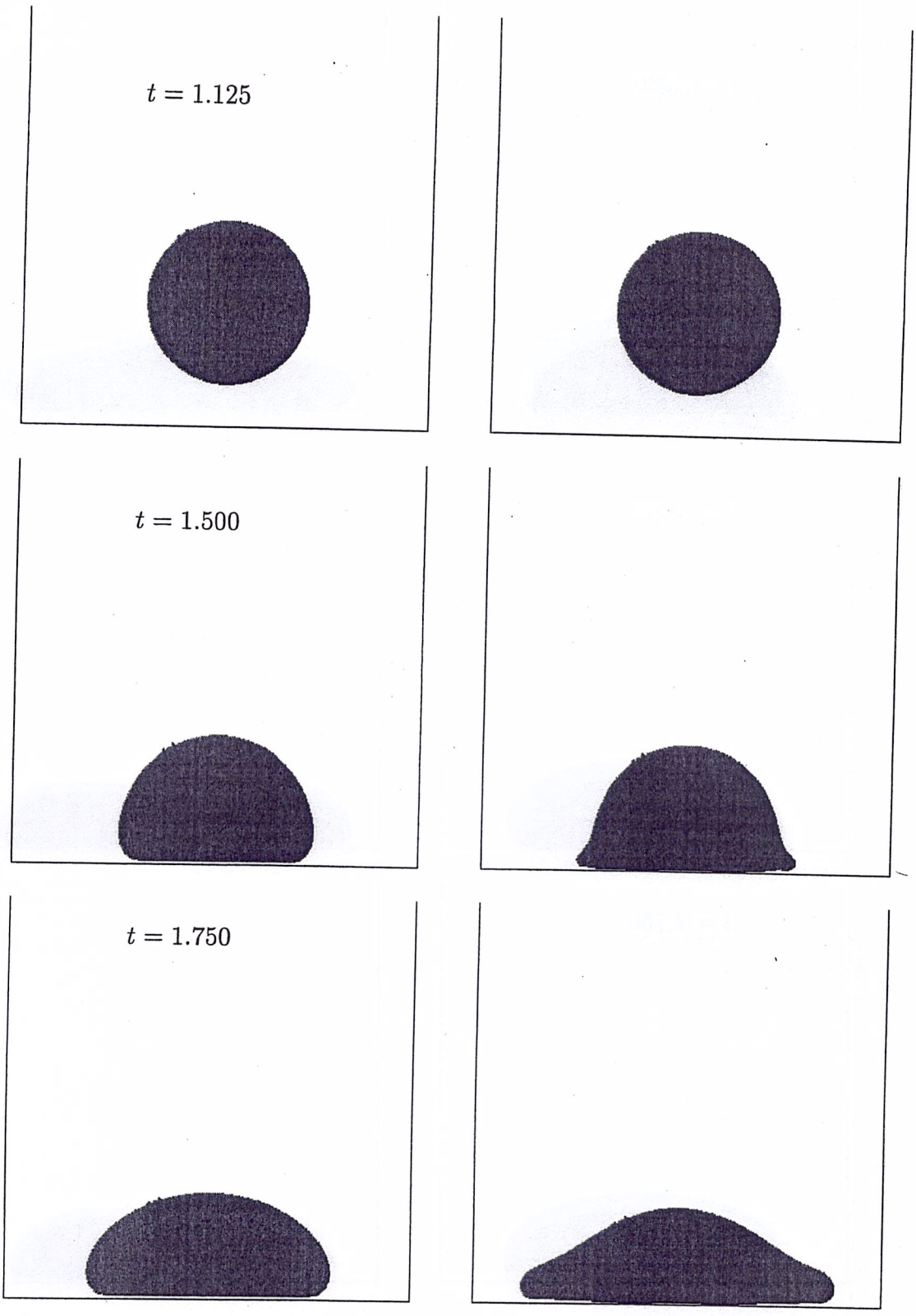

Figure 26. Simulation of falling drops of Newtonian (on the left) and viscoelastic (on the right) fluids. Fluid flow visualization at different times. .

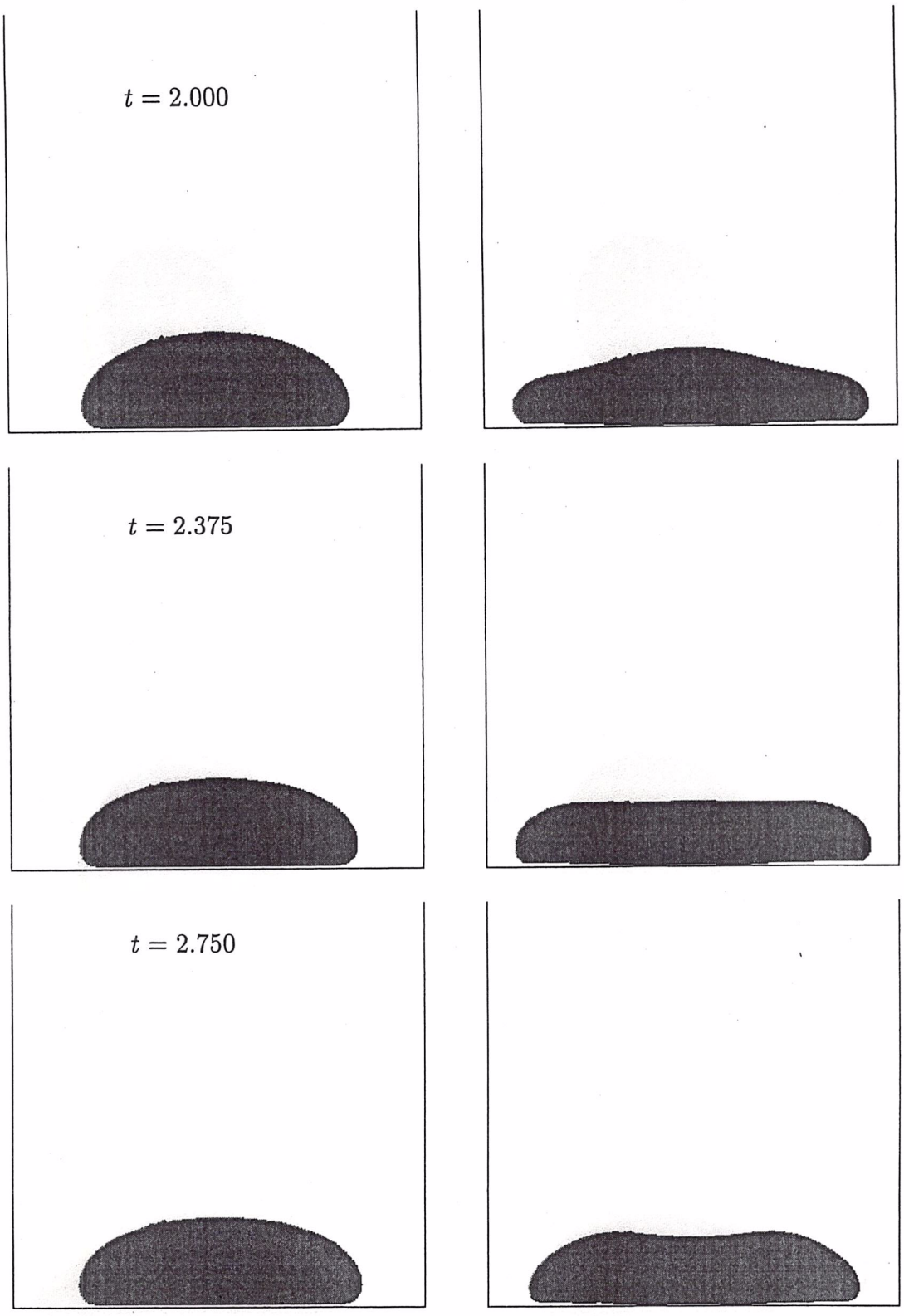

Figure 26. Continued.

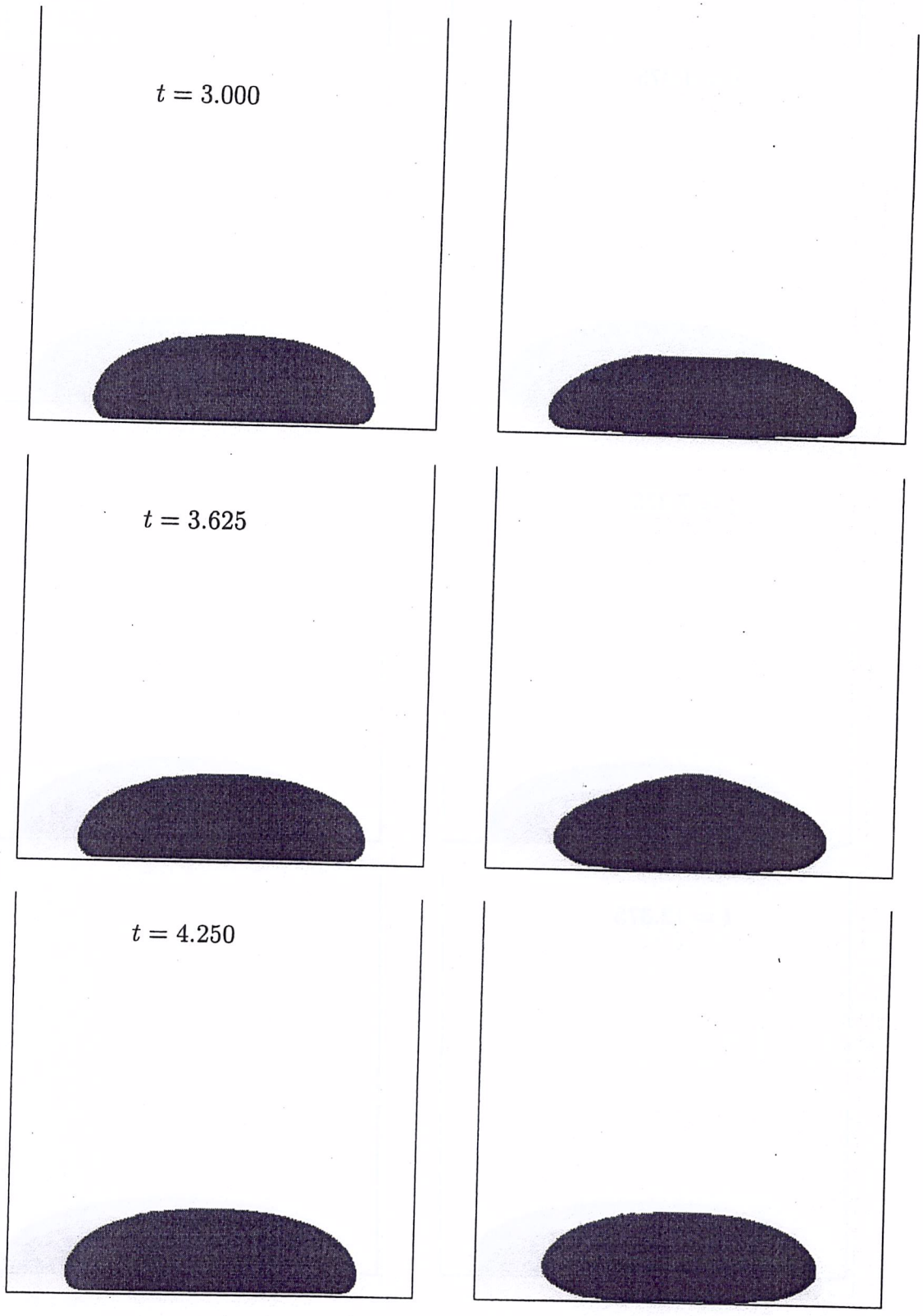

Figure 26. Continued.

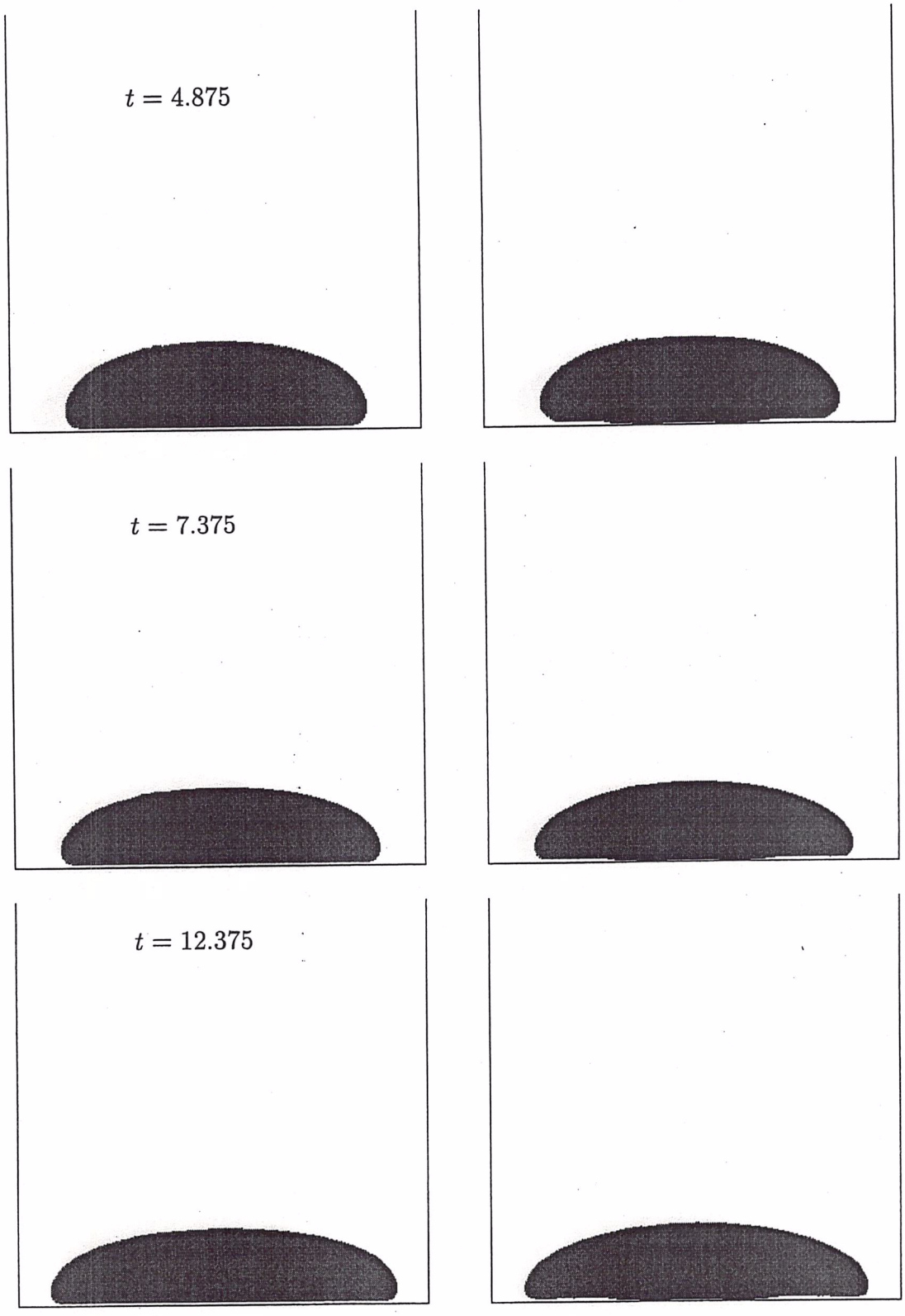

Figure 26. Continued.

Concluding Remarks

This paper has been concerned with the development of a numerical method for solving viscoelastic free surface flows. The finite difference method described has been influenced by the marker and cell methods that originated from Los Alamos in the sixties and seventies. Nonetheless the approach presented here has been highly developed incorporating automatic time stepping and a complete shell that permits output in three dimensional graphic form (in general), that is a video sequence. In particular, this paper has dealt with how we obtain appropriate boundary conditions for the non-Newtonian part of the extra-stress tensor and these derivations have been validated against known analytic expressions. Three examples of viscoelastic flows have been simulated: the classical extrudate swell, viscoelastic jet buckling and the falling viscoelastic fluid drop impinging on a horizontal surface. It is seen that viscoelasticity produces a greater swelling than the Newtonian case as would be anticipated. For viscoelastic jet buckling a wave is seen to travel rapidly back up the jet after impingement causing the jet to buckle much earlier than the corresponding Newtonian case. Jet buckling, whether it be a Newtonian fluid or otherwise, depends upon the accuracy of the computation. The analogy is with flow in a pipe: transition to turbulence is dependent upon the internal surface roughness. Similarly, with a jet the transition to buckling is sensitively dependent upon the degree of precision with which the inlet nozzle is manufactured (see Tome et al. [37]). Thus not only is it not surprising that jet buckling is dependent on the accuracy of the computation; it is to be expected - a small perturbation (round-off error) is necessary to initiate this physical instability. In the viscoelastic case an elastic lateral wave travels back up the jet after impingement causing a large perturbation and almost immediate buckling. Finally the viscoelastic drop falling on to a horizontal surface could be dough thrown on a pastry tray: it deforms in a very distinct manner before relaxing to roughly the same profile as a Newtonian fluid.

We believe this paper is the first serious attempt to solve the Oldroyd B model of unsteady viscoelastic fluid flow with a free surface. We are currently modifying the methodology to allow for cyclindrical geometry so as to simulate the rod-climbing effect.

References

1. J.Y. Yoo, Y. Na, A numerical study of the planar contraction flow of a viscoelastic fluid using the SIMPLER algorithm, J. Non-Newtonian Fluid Mech. **30** (1991) 89-106.

2. J.M. Marchal, M.J. Crochet, A new mixed finite element for calculating viscoelastic flow, J. Non-Newtonian Fluid Mech. **26** (1987) 77-114.

3. E.O.A. Carew, P. Townsend, M.F. Webster, A Taylor-Petrov-Galerkin algorithm for viscoelastic flow, J. Non-Newtonian Fluid Mech. **50** (1993) 253-287.

4. E. Brasseur, M.M. Fyrillas, G.C. Georgiou, M.J. Crochet, The time-dependent extrudate-swell problem of an Oldroyd-B fluid with slip along the wall, J. Rheol. **42** (1998), No.

3, 549-566.

5. X. Huang, N. Phan-Thien, R.I. Tanner, Viscoelastic flow between eccentric rotating cylinders: Unstructured control volume method, J. Non-Newtonian Fluid Mech. **64** (1996) 71-92.

6. G. Mompean, M. Deville, Unsteady finite volume of Oldroyd-B fluid through a three-dimensional planar contraction, J. Non-Newtonian Fluid Mech., **72** (1997) 253-279.

7. S.C. Xue, N. Phan-Thien, R.I. Tanner, Three-dimensional numerical simulation of viscoelastic flows through planar contractions, J. Non-Newtonian Fluid Mech., **74** (1998) 195-245.

8. T.N. Phillips, A.J. Williams, Viscoelastic flow through a planar contraction using a semi-Lagrangian finite volume method, J. Non-Newtonian Fluid Mech., **87** (1999) 215-246.

9. A.N. Beris, R.C. Armstrong, R.A. Brown, Spectral finite-element calculations of the flow of a Maxwell fluid between excentric rotating cylinders, J. Non-Newtonian Fluid Mech., **22** (1987) 129-167.

10. X.J. Fan, N. Phan-Thien, R.Zheng, A direct simulation of fibre suspensions, J. Non-Newtonian Fluid Mech., **74** (1998) 113-135.

11. F. Harlow, J.E. Welch, Numerical Calculation of time-dependent viscous incompressible flow of fluid with a free surface, Phys. Fluids **8** (1965) 2182-2189.

12. M.F. Tomé, S. McKee, GENSMAC: A computational marker-and-cell method for free surface flows in general domains, J. Comput. Phys. **110** (1994) 171-186.

13. A. Castelo, M.F. Tomé, C.N.L. César, S. McKee, J.A. Cuminato, Freeflow: An integrated simulation system for three-dimensional free surface flows, Computing and Visualization in Science, **2** (2000) 199-210.

14. M.F. Tomé, A. Castelo, J. Murakami, J.A. Cuminato, R. Minghim, M.C.F. Oliveira, N. Mangiavacchi, S. McKee, Numerical simulation of axisymmetric free surface flows, J. Comput. Phys. **157** (2000) 441-472.

15. S. Osher and J.A. Sethian, Fronts propagating with curvature-dependent speed: algorithms based on Hamilton-Jacobi formulations, J. Comput. Phys. **79** (1988) 1-49.

16. J.A. Sethian, Theory, algorithms and applications of level Set methods for propagating interfaces, Acta Numerica: C.U.P., Cambridge, UK 1995.

17. J.A. Sethian, Level set methods: Evolving interfaces in geometry, fluid mechanics, Computer Vision and Material Sciences: C.U.P., Cambridge, U.K. 1996.

18. C.W. Hirt, Flow-3D Users Manual, Flow Sciences Inc. 1988.

19. E.G. Puckett, S. Almgren, J.B. Bell, D.L. Marcus, W.J. Rider, A high-order projection method for tracking fluid interfaces in variable density incompressible flows, J. Comput. Phys. **130** (1997) 269-282.

20. M.F. Tomé, A. Castelo, J.A. Cuminato, S. McKee, GENSMAC3D: A numerical method for solving three-dimensional free surface flows, Intern. J. Numer. Meth. Fluids (to appear).

21. H.N. Oguz, A. Prosperetti, Dynamics of bubble growth and detachment from a needle, J. Fluid Mech. **257** (1993), 111-145.

22. J. Glimm, O. McBryan, A computational model for interfaces, Adv. Appl. Math. **6** (1985), 422-435.

23. G. Agresar, J.J. Linderman, G. Tryggvason, K.G. Powell, An adaptive Cartesian front tracking method for the motion, deformation and adhesion of circulating cells, J. Comput. Phys. **143** (1998), 346-380.

24. H.S. Udaykumar, C.H. Kan, W. Shyy, R. Tran-Son-Tay, Multiphase dynamics in arbitrary geometries on fixed Cartesian grids, J. Comput. Phys. **137** (1997), 366-405.

25. M.F. Tomé, B. Duffy and S. McKee, A numerical technique for solving unsteady non-Newtonian free surface flows, *J. Non-Newtonian Fluid Mech.*, **62** (1996), 9-34.

26. M. Crochet, Davis and K. Walters, Numerical Simulation of Non-Newtonian Flow, Elsevier, New York (1984).

27. G.K. *Batchelor, An Introduction to Fluid Dynamics*, Cambridge Univ. Press, Cambridge, 1967.

28. A. Varonos and G. Bergeles, Development and assessment of a variable-order non-oscillatory scheme for convection term discretization, *Intern. J. Numer. Meth. Fluids*, **26** (1998), 1-16.

29. V.G. Ferreira, M. F. Tomé, N. Mangiavacchi,A. Castelo, J. A. Cuminato, A. Fortuna, S. McKee, *High Order Upwinding and the Hydraulic Jump*, Intern. J. Numer. Meth. Fluids (to appear).

30. J.J. Van Schaftingen, Méthodes dél'ements finis pour les écoulements viscoélastistiques, Thése de Doctorat, Université Catholique de Louvain, Louvain-la-Neuve, (1985).

31. J.O. Cruickshank, *Low-Reynolds-number Instabilities in Stagnating Jet Flows*, J. Fluid. Mech. **193** (1988), 111–127.

32. J.O. Cruickshank and B.R. Munson, Viscous-Fluid buckling of plane and axisymmetric jets, J. Fluid Mech., **113** (1981), 221-239.

33. M. F. Tomé and S. McKee, Numerical Simulation of Viscous Flow: Buckling of Planar Jets, Intern. J. Numer. Meth. Fluids, **29** (1999), 705–718.

34. M.J. Crochet and R. Keunings, Die Swell of a Maxwell fluid - Numerical Prediction, J. Non-Newtonian Fluid Mech. **7** (1980), 199-212.

35. C.J. Coleman, Note on Stick-slip and die-swell problems for a second order fluid, J. Non-Newtonian Fluid Mech. **3** (1978), 288-292.

36. G.C. Georgiu and M.J. Crochet, Time-Dependent compressible extrudate-swell problem with slip at the wall, J. Rheology **38:(6)** (1994), 1745-1755.

37. M. F. Tome, S. McKee, L. Barrat, D. A. Jarvis and A. J. Patrick, An Experimental and Numerical Investigation of Container Filling: Liquid fluids, Intern. J. Numer. Meth. Fluids, vol. 31, pag. 1333-1353 (1999).

NOTAS DO ICMC

SÉRIE COMPUTAÇÃO

062/2001 VARGAS, A J C; NONATO, L G. - β-conexão: uma família de objetos tridimensionais reconstruídos a partir de seções planares.

061/2001 OLIVEIRA JR., O N; MARTINS, R T; RINO, L H M ; NUNES, M G V – O uso de interlínguas para comunicação via internet: o projeto UNL/Brasil.

060/2001 SILVA, E Q ; MOREIRA, D A – Use of software agents to the management of distance education courses over the internet.

059/2001 OLIVEIRA, M.C.F.; LEVKOWITZ, H. – Visual data exploration and mining: a survey.

058/2001 SOARES, M D.; FORTES, R P M; MOREIRA, D A – Version–web : a tool for helping web pages version control.

057/2001 LIANG, Z; MACAU, E E N; OMAR, N - Scene Segmentation of the Chaotic Oscillator Network.

056/2000 BATISTA, G E A P A; CARVALHO, A C P L F; MONARD, M C – Applying one-sided selection to unbalanced datasets.

055/2000 NONATO, L G; MINGHIM, R.; OLIVEIRA, M C F; TAVARES, G. – A novel approach for delaunay 3D reconstruction with a comparative analysis in the light of applications.

054/2000 MORSELLI JR., J C M; SANTANA, R H C; SANTANA, M J; ULSON, R S – An approach for dynamic swapping of distributed simulation synchronisation protocols.

053/2000 SPOLON, R.; SANTANA, M J; SANTANA, R H C – A methodology for performance evaluation of optimistic distributed simulation synchronisation mechanisms.